Int J Fract (2017) 208:53–78
https://doi.org/10.1007/s10704-017-0211-5

IUTAM BALTIMORE

Finsler-geometric continuum dynamics and shock compression

J. D. Clayton

Received: 12 October 2016 / Accepted: 11 April 2017 / Published online: 26 April 2017

Abstract A continuum mechanics theory of deformable solids is formulated to account for large deformations, nonlinear elasticity, inelastic deformation mechanisms, microstructure changes, and time dependent fields, i.e., dynamics. The theory incorporates notions from Finsler differential geometry, and it provides a diffuse interface description of surfaces associated with microstructure. Mechanisms include phase transitions and inelastic shearing, with phase boundaries and shear planes the associated surfaces. A director or internal state vector of pseudo-Finsler space is viewed as an order parameter. Newly derived in the present work are the governing equations for dynamics, including kinematic relations, balances of momentum and energy, and evolution law(s) for the internal state. Also derived are jump conditions pertinent to shock loading. Metric tensors and volume can vary isotropically with internal state via a conformal transformation. The dynamic theory is applied to describe shock loading of ceramic crystals of boron carbide, accounting for inelastic mechanisms of shear accommodation and densification upon amorphization under high pressure loading. Analytical predictions incorporating the pseudo-Finsler metric demonstrate remarkable agreement with experimental data, without parameter fitting. Additional solutions suggest that dynamic shear strength could be improved significantly in boron-based ceramics by increasing surface energy, decreasing inelastic shear accommodation in softened amorphous bands, and to a lesser extent, by increasing the energy barrier for phase transformation.

Keywords Continuum mechanics · Differential geometry · Shock physics · Dynamic fracture · Phase field · Ceramics

Invited article for IUTAM Special Issue of *International Journal of Fracture*.

J. D. Clayton (✉)
Visiting Faculty, Department of Civil Engineering and Engineering Mechanics, Columbia University, New York, NY 10027, USA
e-mail: jdc2212@columbia.edu; jdclayt1@umd.edu; john.d.clayton1.civ@mail.mil

J. D. Clayton
A. James Clark School of Engineering, University of Maryland, College Park, MD 20742, USA

J. D. Clayton
Impact Physics, US ARL, Aberdeen, MD 21005-5066, USA

1 Introduction

Crystalline solids may demonstrate a number of inelastic deformation and failure mechanisms under intense dynamic loading. These mechanisms include crystallographic slip (i.e., dislocation glide), deformation twinning, adiabatic shear localization, phase transformations, dynamic cleavage and intergranular fracture, and nucleation, growth, and coalescence of voids. Efforts towards modeling the physics of such phenomena in the context of continuum constitutive theory and numeri-

cal simulations have witnessed incremental progress for several decades. Models for continuum crystal plasticity at high strain rates include (Clayton 2005a; Luscher et al. 2013; Lloyd et al. 2014a; Shahba and Ghosh 2016). Models for deformation twinning include pseudo-slip approaches (Barton et al. 2009; Clayton 2009) and phase field approaches (Clayton and Knap 2011a, 2013, 2015a; Hildebrand and Miehe 2012). Theoretical and computational continuum mechanics models have been developed accounting for shear localization (Li et al. 2001; Bronkhorst et al. 2006; Sun and Mota 2014) and ductile damage, i.e., void mechanics (Bammann and Solanki 2010; Bronkhorst et al. 2016). Phase field theory has also been applied to describe solid-solid phase transformations in the context of finite deformations (Levitas et al. 2009; Clayton 2014a; Levitas 2014). Fractures have been modeled via a number of computational schemes, including cohesive zone methods (Xu and Needleman 1994; Li and Wang 2004; Clayton 2005b; Vogler and Clayton 2008; Foulk and Vogler 2010) and phase field representations (Borden et al. 2012; Clayton and Knap 2014, 2015b).

The current paper invokes a Finsler-geometric theory of continuum mechanics (Clayton 2016a, b, 2017a, b) to account for nonlinear elasticity, inelasticity, and microstructure evolution under dynamic loading conditions. In the context of geometrically nonlinear continuum physics, the body manifold in its referential and spatial configurations is treated as a Finsler space rather than a Euclidean space of conventional continuum mechanics. The metric tensor and its derivative quantities such as lengths, areas, and volumes all functionally depend on an internal state vector or director vector. More precisely, in the present class of theory (Clayton 2016a, b, 2017a, b), each configuration is considered of pseudo-Finsler geometry since the internal state vector need not be a unit vector and the metric need not be homogeneous of degree zero with respect to internal state (Minguzzi 2014). In this work, as first proposed in Clayton (2016a, 2017a), a conformal transformation, i.e., Weyl scaling (Weyl 1952), is used to account for dependence of the metric on internal state. Prior work in the context of quasi-static loading conditions has demonstrated similarities between this class of Finsler theory (Clayton 2016a) and variational phase field models (Clayton and Knap 2015a) when the internal state is regarded as an order parameter. Historically, work in Finsler geometry applied to solid mechanics is limited in scope: the ferromagnetic theory of Amari (1962), kinematic models of Bejancu (1990), and a more comprehensive thermomechanical theory with a numerical example in Saczuk (1996), Stumpf and Saczuk (2000). A recent review of the subject is Clayton (2015a).

As explained in Clayton (2017b), generalized Finsler geometric continuum mechanics includes some distinctive features absent in continuum mechanics models of standard Riemannian geometry. Pseudo-Finsler space invokes basis vectors, metric tensors, and connection coefficients that may explicitly depend on the internal state or director vector. Volume and area elements inherit an explicit state dependence, and Stokes' theorem includes terms accounting for state dependence of connection coefficients in covariant differentiation. Resulting equilibrium equations thereby contain correspondingly novel terms that arise from application of Stokes' theorem. This enriching of the governing equations is thus motivated by mathematical physics rather than ad-hoc constitutive assumptions. Physically, dependence of the metric tensor on internal state is realistic for solid bodies when evolving microstructure alters lengths and/or orientations of material line elements. Finsler geometry is not required for mathematically rigorous modeling of microstructure changes or inelastic deformation, but it does provide an enhanced description relative to standard Riemannian-geometric representations. The present general framework also has been shown (Clayton 2017a) to encompass and reduce to (under certain simplifying assumptions) other classes of continuum models such as those of micropolar (Clayton et al. 2006), strain gradient (Clayton et al. 2004a), and phase field type. Further advantages may become evident upon examination of solutions to specific problems.

The present paper extends previous variational-based (i.e., quasi-static or incremental) theory (Clayton 2016a, b, 2017a, b) to the dynamic regime. Governing equations for dynamics are newly derived: balances of mass, linear momentum, and energy and evolution equation(s) for the internal state. The latter equation(s) are similar in form to those of Ginzburg-Landau or Allen-Cahn phase field theory (Allen and Cahn 1979; Levitas 2014), albeit with additional terms manifesting to account for Finsler space. An important mathematical device used in the current derivations centers on the divergence theorem of Finsler geometry first presented by Rund (1975). Also newly addressed is a Finsler-geometric description of shock wave propaga-

tion in solids. Jump conditions are derived by extending methods in Casey (2011) and Clayton (2014b, c) for Euclidean space to pseudo-Finsler space. In this context, discontinuities in stress, deformation gradient, and particle velocity are assumed to exist across a shock front moving at steady velocity. A linear difference approximation is used to represent state variable gradients across the front, and regions far behind the front are assumed to be in equilibrium with respect to internal state.

The Finsler description of shock physics is used to model planar impact in boron carbide crystals. Boron carbide (B_4C) is a ceramic material of keen current interest. Beneficial physical properties for industrial and defense applications include high hardness, high elastic stiffness, and low mass density. Detrimental properties include low ductility and, under impact loading conditions, a tendency for failure by shear localization. Stress induced amorphization is thought to precede and/or accompany this failure mechanism. Shear banding is a prominent inelastic deformation mechanism in metallic glasses as well (Cheng and Ghosh 2013). The mechanism of amorphization in B_4C is thought related to collapse of the rhombohedral unit cell under compression along the c-axis ([0001] in hexagonal Miller indices) and is further enabled by shearing modes (Grady 2011; Taylor et al. 2012; Clayton 2012a, 2013a, 2014a; Taylor 2015; An and Goddard 2015a).

Prior work applied (Clayton 2016b, 2017b) a static version of Finsler theory to describe tension, compression, and shear of boron carbide single crystals. In this paper, the dynamic version of Finsler theory is newly applied to shock compression of this ceramic. An order parameter is linked simultaneously to densification and inelastic shear accommodation as the crystal transitions to a glassy phase under intense dynamic loading. Analytical solutions are derived in terms of a set of algebraic equations that may be solved simultaneously (albeit, not in closed form) for the shock stress, order parameter, entropy, and shock characteristics such as shock velocity and particle velocity. In addition to modeling the response of the nominal material, the current solutions are used to probe effects of changes in fundamental material properties on dynamic shock stress and dynamic shear strength, the latter of high importance in the context of resistance of ceramic materials to ballistic penetration (Curran et al. 1993; Bourne 2008; Clayton and Tonge 2015; Clayton 2015b, 2016c). Such studies are motivated by concurrent efforts at computational materials design (e.g., via atomic simulations) of boron-based ceramics for improved ductility and failure resistance, for example alloying with boron suboxide (An and Goddard 2015b; Tang et al. 2015).

The remainder of this paper is organized as follows. Section 2 presents the general theory for continuum dynamics in the absence of discontinuities, including differential geometry, kinematics, thermodynamics, and balance laws. Section 3 develops the conservation or jump conditions for a solid domain through which a shock wave propagates at a steady material velocity. Section 4 reports application of the dynamic theory to planar shock loading of B_4C. Section 5 contains concluding remarks.

Notation of continuum physics and Finsler geometry is used. For coordinate-free descriptions, bold type is used for vectors and tensors, and italic type is used for scalars and scalar components. Index notation is frequently invoked with the usual Einstein convention for summation over repeated contravariant and covariant pairs.

2 Theory

Finsler-geometric descriptions of reference and spatial configurations are given, followed by a description of motion of the body. Mathematical aspects discussed already in prior work (Clayton 2016b, 2017a, b) are presented only in brief. Kinematics are further developed to account for time dependency, e.g., velocities and deformation rates. Thermodynamic principles and corresponding balance laws are then newly defined or derived for the dynamic case.

2.1 Pseudo-Finsler geometry

Finsler geometric representations of reference and spatial configurations are given in Sects. 2.1.1 and 2.1.2. Mappings between such configurations are then discussed in Sect. 2.1.3. Rate kinematics are defined in Sect. 2.1.4. Multiplicative decompositions of the deformation gradient and metric tensors are introduced in Sect. 2.1.5.

2.1.1 Reference configuration

Let $\mathfrak{M}$ be a differential manifold of spatial dimension 3. Let $X \in \mathfrak{M}$ denote a material point, and let

$\{X^A\}(A = 1, 2, 3)$ denote a coordinate chart covering part or all of $\mathfrak{M}$. To each point is assigned a vector $\boldsymbol{D}$ serving as a descriptor of possibly evolving microstructure. Coordinates $\{D^A\}(A = 1, 2, 3)$ are the entries of $\boldsymbol{D}$. The vector $\boldsymbol{D}$, called a state vector or internal state vector, need not be of unit length, thought it may be referred to as a director vector regardless. In notational arguments, dependence of a function on $(\boldsymbol{X}, \boldsymbol{D})$ implies dependence on reference charts $(\{X^A\}, \{D^A\})$.

Holonomic basis vectors are the fields $\{\frac{\partial}{\partial X^A}, \frac{\partial}{\partial D^A}\}$. Let $N_B^A(\boldsymbol{X}, \boldsymbol{D})$ denote nonlinear connection coefficients. In Finsler geometry, the non-holonomic basis whose entries transform between coordinate systems as typical vectors is

$$\frac{\delta}{\delta X^A} = \frac{\partial}{\partial X^A} - N_A^B \frac{\partial}{\partial D^B}, \quad \delta D^A = dD^A + N_B^A dX^B. \tag{2.1}$$

The set $\{\frac{\delta}{\delta X^A}, \frac{\partial}{\partial D^A}\}$ is logically used for a local basis on the referential tangent bundle, and the reciprocal set $\{dX^A, \delta D^A\}$ for the cotangent bundle. The Sasaki metric is

$$\begin{aligned}\boldsymbol{G}(\boldsymbol{X}, \boldsymbol{D}) &= G_{AB}(\boldsymbol{X}, \boldsymbol{D}) dX^A \otimes dX^B \\ &\quad + G_{AB}(\boldsymbol{X}, \boldsymbol{D}) \delta D^A \otimes \delta D^B.\end{aligned} \tag{2.2}$$

Components G_{AB} (G^{AB}) are used to lower (raise) indices, and the determinant is $G(\boldsymbol{X}, \boldsymbol{D}) = \det[G_{AB}(\boldsymbol{X}, \boldsymbol{D})]$. Partial coordinate differentiation and delta-differentiation are written as

$$\begin{aligned}&\partial_A(\cdot) = \frac{\partial(\cdot)}{\partial X^A}, \quad \bar{\partial}_A(\cdot) = \frac{\partial(\cdot)}{\partial D^A}; \\ &\delta_A(\cdot) = \frac{\delta(\cdot)}{\delta X^A} = \partial_A(\cdot) - N_A^B \bar{\partial}_B(\cdot).\end{aligned} \tag{2.3}$$

The Christoffel symbols of the second kind for the Levi-Civita connection on $\mathfrak{M}$ are

$$\begin{aligned}\gamma_{BC}^A &= \tfrac{1}{2} G^{AD}(\partial_C G_{BD} + \partial_B G_{CD} - \partial_D G_{BC}) \\ &= G^{AD} \gamma_{BCD}.\end{aligned} \tag{2.4}$$

Cartan's tensor referred to reference coordinates is

$$\begin{aligned}C_{BC}^A &= \tfrac{1}{2} G^{AD}(\bar{\partial}_C G_{BD} + \bar{\partial}_B G_{CD} - \bar{\partial}_D G_{BC}) \\ &= G^{AD} C_{BCD}.\end{aligned} \tag{2.5}$$

The horizontal coefficients of the Chern-Rund and Cartan connections are both equal to

$$\begin{aligned}\Gamma_{BC}^A &= \tfrac{1}{2} G^{AD}(\delta_C G_{BD} + \delta_B G_{CD} - \delta_D G_{BC}) \\ &= G^{AD} \Gamma_{BCD}.\end{aligned} \tag{2.6}$$

The spray and its canonical nonlinear connection coefficients, with the latter an example of those in (2.1) when $N_B^A = G_B^A$, are, respectively,

$$G^A = \tfrac{1}{2} \gamma_{BC}^A D^B D^C, \qquad G_B^A = \bar{\partial}_B G^A. \tag{2.7}$$

Denote by ∇ the covariant derivative. Horizontal gradients of basis vectors are

$$\begin{aligned}\nabla_{\delta/\delta X^B} \frac{\delta}{\delta X^C} &= H_{BC}^A \frac{\delta}{\delta X^A}, \\ \nabla_{\delta/\delta X^B} \frac{\partial}{\partial D^C} &= K_{BC}^A \frac{\partial}{\partial D^A},\end{aligned} \tag{2.8}$$

with coefficients H_{BC}^A and K_{BC}^A. Vertical gradients of basis vectors are similarly obtained from coefficients V_{BC}^A and Y_{BC}^A:

$$\begin{aligned}\nabla_{\partial/\partial D^B} \frac{\partial}{\partial D^C} &= V_{BC}^A \frac{\partial}{\partial D^A}, \\ \nabla_{\partial/\partial D^B} \frac{\delta}{\delta X^C} &= Y_{BC}^A \frac{\delta}{\delta X^A}.\end{aligned} \tag{2.9}$$

The above descriptions pertain to both pseudo-Finsler space and Finsler space. The latter type of space is a subset of the former, and conditions for which a pseudo-Finsler space is a strict Finsler space are discussed elsewhere (Minguzzi 2014; Clayton 2016a). Two connections often encountered in the (pseudo)-Finsler literature are (Minguzzi 2014)

- Chern-Rund connection: $N_B^A = G_B^A, H_{BC}^A = K_{BC}^A = \Gamma_{BC}^A, V_{BC}^A = Y_{BC}^A = 0$;
- Cartan connection: $N_B^A = G_B^A, H_{BC}^A = K_{BC}^A = \Gamma_{BC}^A, V_{BC}^A = Y_{BC}^A = C_{BC}^A$.

Let $(\cdot)_{|C}$ denote horizontal covariant differentiation in a coordinate chart $\{X^C\}$. Then when either of these two connections is used, the horizontal covariant derivative $G_{AB|C} = 0$.

Denote by $\mathrm{d}\boldsymbol{X}$ and and $\mathrm{d}\boldsymbol{D}$ differential line or vector elements. Squared differential line lengths with respect to (2.2) are

$$\begin{aligned}|\mathrm{d}\boldsymbol{X}|^2 &= \langle \mathrm{d}\boldsymbol{X}, \boldsymbol{G}\mathrm{d}\boldsymbol{X} \rangle = G_{AB} \mathrm{d}X^A \mathrm{d}X^B, \\ |\mathrm{d}\boldsymbol{D}|^2 &= \langle \mathrm{d}\boldsymbol{D}, \boldsymbol{G}\mathrm{d}\boldsymbol{D} \rangle = G_{AB} \mathrm{d}D^A \mathrm{d}D^B.\end{aligned} \tag{2.10}$$

Scalar volume elements and volume forms of $\mathfrak{M}$ are Rund (1975)

$$\begin{aligned}\mathrm{d}V &= \sqrt{G} \mathrm{d}X^1 \mathrm{d}X^2 \mathrm{d}X^3, \\ d\Omega &= \sqrt{G} \mathrm{d}X^1 \wedge \mathrm{d}X^2 \wedge \mathrm{d}X^3.\end{aligned} \tag{2.11}$$

The differential area form corresponding to a compact region of $\mathfrak{M}$ is

$$\Omega = \sqrt{\beta}\mathrm{d}U^1 \wedge \mathrm{d}U^2; \quad \left[X^A = X^A(U^\alpha),\ (\alpha = 1, 2);\right.$$
$$\left.\beta^A_\alpha = \frac{\partial X^A}{\partial U^\alpha}, \quad \beta = \det(\beta^A_\alpha G_{AB}\beta^B_\beta)\right] \tag{2.12}$$

The following identities apply for gradients of G:

$$\delta_A(\ln\sqrt{G}) = \Gamma^B_{AB},$$
$$(\sqrt{G})_{|A} = \partial_A(\sqrt{G}) - N^B_A\bar{\partial}_B(\sqrt{G}) - \sqrt{G}H^B_{AB}. \tag{2.13}$$

Let $V^A(\boldsymbol{X}, \boldsymbol{D})\Omega(\boldsymbol{X}, \boldsymbol{D})$ be a 2-form, and let V^A be contravariant components of generic differentiable vector field $\boldsymbol{V} = V^A\frac{\delta}{\delta X^A}$. Prescribe the horizontal connection as one for which $H^B_{AB} = \Gamma^B_{AB} \Rightarrow (\sqrt{G})_{|A} = 0$. Then in a coordinate chart $\{X^A\}$, Stokes' theorem is Rund (1975)

$$\int_{\mathfrak{M}}[V^A_{|A} + (V^A C^C_{BC} + \bar{\partial}_B V^A)D^B_{;A}]d\Omega$$
$$= \oint_{\partial\mathfrak{M}} V^A N_A \Omega. \tag{2.14}$$

Here, N_A is the unit outward normal to $\partial\mathfrak{M}$, $V^A_{|A} = \delta_A V^A + V^A H^B_{BA}$, and $D^B_{;A} = \partial_A D^B + N^B_A$. Motivated by this theorem, a covariant derivative operation $(\cdot)_{||A}$ is defined in a reference coordinate chart as

$$(\cdot)_{||A} = (\cdot)_{|A} + [(\cdot)C^C_{BC} + \bar{\partial}_B(\cdot)]D^B_{;A}$$
$$\Rightarrow \quad \int_{\mathfrak{M}}(\cdot)_{||A}d\Omega = \oint_{\partial\mathfrak{M}}(\cdot)N_A\Omega. \tag{2.15}$$

In other words, (2.15) enables presentation of Stokes' theorem (including the divergence theorem of Rund Rund (1975)) in Finsler geometry in a compact form comparable to that in Riemannian geometry (Clayton 2014d).

2.1.2 Spatial configuration

The spatial configuration corresponds to a time t at which the solid has undergone motion. A pseudo-Finsler geometric framework exists that exactly parallels Sect. 2.1.1. Notation provides the distinction: deformed coordinates and their indices are written in lower-case rather than capitals.

Differential manifold $\mathfrak{m}$ of spatial dimension 3 describes the body embedded in ambient Euclidean 3-space. Let $x \in \mathfrak{m}$ denote a spatial point, and let $\{x^a\}(a = 1, 2, 3)$ denote a chart on $\mathfrak{m}$. Attached to each point is the internal state vector $\boldsymbol{d}$, with secondary coordinates $\{d^a\}(a = 1, 2, 3)$; $\boldsymbol{d}$ need not be a unit vector. The natural or holonomic basis is $\{\frac{\partial}{\partial x^a}, \frac{\partial}{\partial d^a}\}$. With $n^a_b(\boldsymbol{x}, \boldsymbol{d})$ spatial nonlinear connection coefficients, the usual non-holonomic basis vectors are

$$\frac{\delta}{\delta x^a} = \frac{\partial}{\partial x^a} - n^b_a\frac{\partial}{\partial d^b}, \qquad \delta d^a = dd^a + n^a_b dx^b. \tag{2.16}$$

The set $\{\frac{\delta}{\delta x^a}, \frac{\partial}{\partial d^a}\}$ will be used as a local basis over the spatial tangent bundle, and $\{dx^a, \delta d^a\}$ for the cotangent bundle. The spatial Sasaki metric tensor is

$$\boldsymbol{g}(\boldsymbol{x}, \boldsymbol{d}) = g_{ab}(\boldsymbol{x}, \boldsymbol{d})dx^a \otimes dx^b + g_{ab}(\boldsymbol{x}, \boldsymbol{d})\delta d^a \otimes \delta d^b, \tag{2.17}$$

with determinant $g(\boldsymbol{x}, \boldsymbol{d}) = \det[g_{ab}(\boldsymbol{x}, \boldsymbol{d})]$. Spatial differentiation follows the notation

$$\partial_a(\cdot) = \frac{\partial(\cdot)}{\partial x^a}, \quad \bar{\partial}_a(\cdot) = \frac{\partial(\cdot)}{\partial d^a};$$
$$\delta_a(\cdot) = \frac{\delta(\cdot)}{\delta x^a} = \partial_a(\cdot) - n^b_a\bar{\partial}_b(\cdot). \tag{2.18}$$

Levi-Civita connection coefficients on $\mathfrak{m}$ are

$$\gamma^a_{bc} = \tfrac{1}{2}g^{ad}(\partial_c g_{bd} + \partial_b g_{cd} - \partial_d g_{bc}) = g^{ad}\gamma_{bcd}. \tag{2.19}$$

Cartan's tensor is

$$C^a_{bc} = \tfrac{1}{2}g^{ad}(\bar{\partial}_c g_{bd} + \bar{\partial}_b g_{cd} - \bar{\partial}_d g_{bc}) = g^{ad}C_{bcd}. \tag{2.20}$$

Horizontal coefficients of Chern-Rund and Cartan connections are

$$\Gamma^a_{bc} = \tfrac{1}{2}g^{ad}(\delta_c g_{bd} + \delta_b g_{cd} - \delta_d g_{bc}) = g^{ad}\Gamma_{bcd}. \tag{2.21}$$

The spray and canonical nonlinear connection coefficients (when $n^a_b = g^a_b$) are

$$g^a = \tfrac{1}{2}\gamma^a_{bc}d^b d^c, \qquad g^a_b = \bar{\partial}_b g^a. \tag{2.22}$$

Horizontal gradients of basis vectors are found from connection coefficients H^a_{bc} and K^a_{bc}:

$$\nabla_{\delta/\delta x^b}\frac{\delta}{\delta x^c} = H^a_{bc}\frac{\delta}{\delta x^a}, \qquad \nabla_{\delta/\delta x^b}\frac{\partial}{\partial d^c} = K^a_{bc}\frac{\partial}{\partial d^a}. \tag{2.23}$$

Vertical connection coefficients V^a_{bc} and Y^a_{bc} yield vertical gradients:

$$\nabla_{\partial/\partial d^b}\frac{\partial}{\partial d^c} = V^a_{bc}\frac{\partial}{\partial d^a}, \qquad \nabla_{\partial/\partial d^b}\frac{\delta}{\delta x^c} = Y^a_{bc}\frac{\delta}{\delta x^a}. \tag{2.24}$$

Line and volume elements analogous to those in Sect. 2.1.1 exist, as does an area form ω like Ω in (2.12). Spatial versions of Stokes' theorem (2.14) hold, where in particular, the analog of (2.15) is

$$\begin{aligned}(\cdot)_{||a} &= (\cdot)_{|a} + [(\cdot)C^c_{bc} + \bar\partial_b(\cdot)]d^b_{;a}\\ \Rightarrow \qquad \int_{\mathfrak{m}}(\cdot)_{||a}d\omega &= \oint_{\partial\mathfrak{m}}(\cdot)n_a\omega.\end{aligned} \tag{2.25}$$

2.1.3 Deformation kinematics

The time-dependent motions from $\mathfrak{M}$ to $\mathfrak{m}$ and vice versa are the C^2 functions

$$\begin{aligned}x^a(\boldsymbol{X},\boldsymbol{D},t) &= \varphi^a[\boldsymbol{X},\boldsymbol{D}(\boldsymbol{X},t),t],\\ X^A(\boldsymbol{x},\boldsymbol{d},t) &= \Phi^A[\boldsymbol{x},\boldsymbol{d}(\boldsymbol{x},t),t].\end{aligned} \tag{2.26}$$

Unlike variational theories in prior work (Clayton 2016b, 2017a, b), here time t is an explicit independent variable. Finsler kinematics (Bejancu 1990; Saczuk 1996; Stumpf and Saczuk 2000; Clayton 2017a) may differ from classical finite kinematics in Riemannian geometry via incorporation of internal state in these motion functions. State vector mappings are

$$\begin{aligned}d^a(\boldsymbol{X},\boldsymbol{D},t) &= \theta^a[\boldsymbol{X},\boldsymbol{D}(\boldsymbol{X},t),t],\\ D^A(\boldsymbol{x},\boldsymbol{d},t) &= \Theta^A[\boldsymbol{x},\boldsymbol{d}(\boldsymbol{x},t),t].\end{aligned} \tag{2.27}$$

The deformation gradient of Finsler-geometric continuum mechanics (Clayton 2016b, 2017a) is defined as the partial derivative of motion referred to the non-holonomic basis:

$$\begin{aligned}\boldsymbol{F}(\boldsymbol{X},\boldsymbol{D},t) &= F^a_A(\boldsymbol{X},\boldsymbol{D},t)\frac{\delta}{\delta x^a}\otimes dX^A\\ &= \frac{\partial\varphi^a(\boldsymbol{X},\boldsymbol{D},t)}{\partial X^A}\frac{\delta}{\delta x^a}\otimes dX^A\\ &= \frac{\partial\boldsymbol{x}(\boldsymbol{X},\boldsymbol{D},t)}{\partial\boldsymbol{X}}, \qquad F^a_A = \partial_A\varphi^a = \partial_A x^a.\end{aligned} \tag{2.28}$$

The inverse tangent mapping from spatial to referential coordinates similarly is

$$\begin{aligned}\boldsymbol{f}(\boldsymbol{x},\boldsymbol{d},t) &= f^A_a(\boldsymbol{x},\boldsymbol{d},t)\frac{\delta}{\delta X^A}\otimes dx^a\\ &= \frac{\partial\Phi^A(\boldsymbol{x},\boldsymbol{d},t)}{\partial x^a}\frac{\delta}{\delta X^A}\otimes dx^a\\ &= \frac{\partial\boldsymbol{X}(\boldsymbol{x},\boldsymbol{d},t)}{\partial\boldsymbol{x}}, \qquad f^A_a = \partial_a\Phi^A = \partial_a X^A.\end{aligned} \tag{2.29}$$

Functions $\boldsymbol{F}$ and $\boldsymbol{f}$ are invertible with positive determinants, and are inverses of one another at coincident points on $\mathfrak{M}$ or $\mathfrak{m}$ at the same time instant t:

$$\begin{aligned}&F^a_A[\boldsymbol{X},\boldsymbol{D}(\boldsymbol{X},t),t]f^A_b[\boldsymbol{x}(\boldsymbol{X},\boldsymbol{D},t),\boldsymbol{d}(\boldsymbol{x}(\boldsymbol{X},\boldsymbol{D},t),t)] = \delta^a_b,\\ &f^A_a[\boldsymbol{x},\boldsymbol{d}(\boldsymbol{x},t),t]F^a_B[\boldsymbol{X}(\boldsymbol{x},\boldsymbol{d},t),\boldsymbol{D}(\boldsymbol{X}(\boldsymbol{x},\boldsymbol{d},t),t)] = \delta^A_B.\end{aligned} \tag{2.30}$$

Director deformation gradients introduced elsewhere (Clayton 2016b) are admissible but inessential to forthcoming derivations.

Similar to those of Riemannian geometry, transformation equations for line elements and volume elements/forms are (Clayton 2016a, b, 2017a, b)

$$\begin{aligned}\mathrm{d}\boldsymbol{x} &= \frac{\partial\boldsymbol{x}}{\partial\boldsymbol{X}}\mathrm{d}\boldsymbol{X} \Leftrightarrow \mathrm{d}x^a = F^a_A\mathrm{d}X^A,\\ \mathrm{d}\boldsymbol{X} &= \frac{\partial\boldsymbol{X}}{\partial\boldsymbol{x}}\mathrm{d}\boldsymbol{x} \Leftrightarrow \mathrm{d}X^A = f^A_a\mathrm{d}x^a;\end{aligned} \tag{2.31}$$

$$\begin{aligned}\mathrm{d}v &= J\mathrm{d}V = [\det(F^a_A)\sqrt{g/G}]\mathrm{d}V,\\ \mathrm{d}V &= j\mathrm{d}v = [\det(f^A_a)\sqrt{G/g}]\mathrm{d}v,\\ d\omega &= Jd\Omega, \quad d\Omega = jd\omega.\end{aligned} \tag{2.32}$$

Lengths of deformed to initial line elements are described by the symmetric deformation tensor $\boldsymbol{C}$:

$$\begin{aligned}|\mathrm{d}\boldsymbol{x}|^2 &= F^a_AF^b_Bg_{ab}\mathrm{d}X^A\mathrm{d}X^B = C_{AB}\mathrm{d}X^A\mathrm{d}X^B\\ &= \langle\mathrm{d}\boldsymbol{X},\boldsymbol{C}\mathrm{d}\boldsymbol{X}\rangle,\\ \boldsymbol{C} &= C_{AB}dX^A\otimes dX^B = F^a_Ag_{ab}F^b_BdX^A\otimes dX^B.\end{aligned} \tag{2.33}$$

It follows that $\det(C^A_B) = \det(C_{AB})/G = J^2$. Mixed horizontal gradients of non-holonomic bases are obtained using (2.3), (2.23), and (2.28):

$$\begin{aligned}\nabla_{\delta/\delta X^A}\frac{\delta}{\delta x^c} &= \frac{\delta x^a}{\delta X^A}\nabla_{\delta/\delta x^a}\frac{\delta}{\delta x^c}\\ &= (F^a_A - N^B_A\bar\partial_Bx^a)\nabla_{\delta/\delta x^a}\frac{\delta}{\delta x^c}\\ &= (F^a_A - N^B_A\bar\partial_Bx^a)H^b_{ac}\frac{\delta}{\delta x^b}.\end{aligned} \tag{2.34}$$

2.1.4 Material time derivatives

The notion of a material time derivative in Finsler space is needed for subsequent derivations in the dynamic Finsler-geometric continuum theory. Let a superposed dot and the notation $D(\cdot)/Dt$ denote the material time derivative, which is defined here as the partial time derivative of a quantity at a fixed material point $\boldsymbol{X}$ and at fixed internal state $\boldsymbol{D}$. For example, let $A(\boldsymbol{X}, \boldsymbol{D}, t)$ denote a generic differentiable field variable; its material time derivative is

$$\dot{A}(\boldsymbol{X}, \boldsymbol{D}, t) = \frac{DA(\boldsymbol{X}, \boldsymbol{D}, t)}{Dt} = \frac{\partial A(\boldsymbol{X}, \boldsymbol{D}, t)}{\partial t}. \tag{2.35}$$

The material velocity (vector) is defined as the material time derivative of position, i.e.,

$$\begin{aligned} \boldsymbol{v}(\boldsymbol{X}, \boldsymbol{D}, t) &= \frac{\partial \boldsymbol{x}(\boldsymbol{X}, \boldsymbol{D}, t)}{\partial t} = \frac{\partial \varphi^a(\boldsymbol{X}, \boldsymbol{D}, t)}{\partial t} \frac{\delta}{\delta x^a}, \\ v^a &= \frac{Dx^a}{Dt}. \end{aligned} \tag{2.36}$$

The material acceleration is the material time derivative of velocity:

$$\begin{aligned} \boldsymbol{a}(\boldsymbol{X}, \boldsymbol{D}, t) &= \frac{\partial \boldsymbol{v}(\boldsymbol{X}, \boldsymbol{D}, t)}{\partial t} = a^a(\boldsymbol{X}, \boldsymbol{D}, t) \frac{\delta}{\delta x^a}, \\ a^a &= \frac{Dv^a}{Dt}. \end{aligned} \tag{2.37}$$

A fundamental assumption is that material time derivatives of Sasaki metric tensors vanish identically, analogously to the same identities that can be derived in Riemannian geometry (Clayton 2014d) where metrics may depend only on coordinates but not internal state:

$$\begin{aligned} &\dot{\boldsymbol{G}}(\boldsymbol{X}, \boldsymbol{D}) = \frac{\partial \boldsymbol{G}(\boldsymbol{X}, \boldsymbol{D})}{\partial t} = 0, \\ &\dot{\boldsymbol{g}}[\boldsymbol{x}(\boldsymbol{X}, \boldsymbol{D}, t), \boldsymbol{d}(\boldsymbol{x}(\boldsymbol{X}, \boldsymbol{D}, t), t)] \\ &= \frac{\partial \boldsymbol{g}[\boldsymbol{x}(\boldsymbol{X}, \boldsymbol{D}, t), \boldsymbol{d}(\boldsymbol{x}(\boldsymbol{X}, \boldsymbol{D}, t), t)]}{\partial t} = 0. \end{aligned} \tag{2.38}$$

This description naturally excludes convected coordinate representations. The first of (2.38) is derived trivially by inspection; the second assumes that a metric-compatible connection describes spatial gradients of basis vectors and that $\boldsymbol{d}$ is held fixed during time differentiation.

The definition of the material time derivative of the deformation gradient, like that of $\boldsymbol{F}$ itself (Bejancu 1990; Stumpf and Saczuk 2000; Clayton 2016a, 2017a), is non-unique in Finsler-geometric continuum mechanics. In the present theory, the rate of deformation gradient is defined as follows:

$$\dot{\boldsymbol{F}}(\boldsymbol{X}, \boldsymbol{D}, t) = \frac{D}{Dt} \boldsymbol{F}(\boldsymbol{X}, \boldsymbol{D}, t) = \boldsymbol{L}(\boldsymbol{X}, \boldsymbol{D}, t) \boldsymbol{F}(\boldsymbol{X}, \boldsymbol{D}, t), \tag{2.39}$$

where $\boldsymbol{L}$ is the velocity gradient tensor:

$$\boldsymbol{L} = L^a_b \frac{\delta}{\delta x^a} \otimes dx^b = v^a_{||b} \frac{\delta}{\delta x^a} \otimes dx^b. \tag{2.40}$$

The covariant derivative operation entering definition (2.40) is defined in (2.25). From (2.38) to (2.40), the time derivative of the Jacobian determinant of (2.32) is

$$\dot{J} = \frac{\partial J}{\partial F^a_A} \dot{F}^a_A = J(F^{-1})^A_a \dot{F}^a_A = J L^a_a = J v^a_{||a}. \tag{2.41}$$

Let Φ denote the volume integral of a generic scalar quantity ϕ over spatial domain ω, with material time derivative $\dot{\Phi}$:

$$\begin{aligned} \Phi(t) &= \int_\omega \phi(\boldsymbol{x}, \boldsymbol{D}, t) d\omega, \\ \dot{\Phi}(t) &= \frac{D}{Dt} \int_\omega \phi(\boldsymbol{x}, \boldsymbol{D}, t) d\omega. \end{aligned} \tag{2.42}$$

The second of (2.42) can be manipulated using (2.25) and (2.41):

$$\begin{aligned} \dot{\Phi} &= \frac{D}{Dt} \int_\Omega \phi J d\Omega = \int_\omega (\dot{\phi} + \phi v^a_{||a}) d\omega \\ &= \int_\omega \left[\left. \frac{\partial \phi}{\partial t} \right|_{\boldsymbol{x}, D} + (\phi v^a)_{||a} \right] d\omega \\ &= \frac{\partial}{\partial t} \left(\int_\omega \frac{\partial \phi}{\partial t} d\omega \right) \Bigg|_{\boldsymbol{x}, D} + \oint_{\partial\omega} (\phi v^a) n_a \omega. \end{aligned} \tag{2.43}$$

In this version of Reynolds' transport theorem extended to Finsler space, the partial derivative of $\phi(\boldsymbol{x}, \boldsymbol{D}, t)$ at fixed $\boldsymbol{x}$ and $\boldsymbol{D}$ is defined as the difference $\partial\phi/\partial t = \dot{\phi} - \phi_{||a} v^a$. Equations (2.35)–(2.43) reduce to their usual counterparts of classical continuum physics (Clayton 2011, 2014d) when $\boldsymbol{D}$ and $\boldsymbol{d}$ are omitted entirely, in which case the respective reference and current configuration manifolds become those of usual Riemannian geometry and Euclidean space in particular.

2.1.5 Multiplicative kinematics

A multiplicative decomposition of the Finsler-geometric deformation gradient of (2.28) is invoked. Let $\boldsymbol{F}$ be decomposed into a product of two non-singular two-point tensors:

$$\boldsymbol{F} = \boldsymbol{F}^E \boldsymbol{F}^D, \qquad F^a_A = (F^E)^a_\alpha (F^D)^\alpha_A. \tag{2.44}$$

Both the thermoelastic or thermomechanically recoverable deformation, $\boldsymbol{F}^E$, and the residual or inelastic deformation associated with changes of internal state, $\boldsymbol{F}^D$, have positive determinants. Functional forms are (Clayton 2016b, 2017b)

$$(F^E)^a_\alpha = (F^E)^a_\alpha(\boldsymbol{X}, t), \quad (F^D)^\alpha_A = (F^D)^\alpha_A[\boldsymbol{D}(\boldsymbol{X}, t)], \tag{2.45}$$

where the inelastic two-point tensor $\boldsymbol{F}^D$ may have further dependence on $\boldsymbol{X}$ only via possible dependence of its basis vectors on $\boldsymbol{X}$. Greek indices correspond to a generally anholonomic space (Clayton 2012b, 2014d) (i.e., incompatible intermediate configuration). Local integrability conditions, or lack thereof, for the total deformation gradient and its constituents are discussed in Clayton (2016b). A multiplicative split of the director gradient function has also been introduced in prior work (Clayton 2016b). As demonstrated in detail in Clayton (2017b), the multiplicative decomposition of deformation is useful for partitioning elastic and inelastic contributions, whereby only the former directly influence the mechanical stress. The inelastic deformation may generally consist of contributions from various structural transformations including plasticity, twinning, phase changes, and damage development. Setting $\boldsymbol{F}^D$ as an explicit function of $\boldsymbol{D}$ enables a kinetic relation or equilibrium equation for the internal state to dictate the evolution of inelastic deformation, eliminating the need to introduce a separate governing equation for the latter.

Multiplicative decompositions of the referential Sasaki metric tensor and its inverse are used later:

$$\begin{aligned} G_{AB}(\boldsymbol{X}, \boldsymbol{D}) &= \bar{G}_{AC}(\boldsymbol{X})\hat{G}^C_B(\boldsymbol{D}), \\ G^{AB}(\boldsymbol{X}, \boldsymbol{D}) &= \bar{G}^{AC}(\boldsymbol{X})(\hat{G}^{-1})^B_C(\boldsymbol{D}). \end{aligned} \tag{2.46}$$

Analogous decompositions into position- and microstructure-dependent parts apply for the spatial metric:

$$\begin{aligned} g_{ab}(\boldsymbol{x}, \boldsymbol{d}) &= \bar{g}_{ac}(\boldsymbol{x})\hat{g}^c_b(\boldsymbol{d}), \\ g^{ab}(\boldsymbol{x}, \boldsymbol{d}) &= \bar{g}^{ac}(\boldsymbol{x})(\hat{g}^{-1})^b_c(\boldsymbol{d}). \end{aligned} \tag{2.47}$$

Another metric tensor is used on the intermediate configuration (Clayton et al. 2004b), split multiplicatively (Clayton 2016b):

$$\begin{aligned} &g_{\alpha\beta}(\boldsymbol{X}, \boldsymbol{D}) = \bar{g}_{\alpha\gamma}(\boldsymbol{X})\hat{g}^\gamma_\beta(\boldsymbol{D}), \\ &g^{\alpha\beta}(\boldsymbol{X}, \boldsymbol{D}) = \bar{g}^{\alpha\gamma}(\boldsymbol{X})(\hat{g}^{-1})^\beta_\gamma(\boldsymbol{D}); \\ &\tilde{g} = \det(g_{\alpha\beta}) = 1/\det(g^{\alpha\beta}). \end{aligned} \tag{2.48}$$

For the total intermediate metric and intermediate structure-independent metric, the following forms (Clayton 2016b) prove most convenient:

$$\begin{aligned} &g_{\alpha\beta}(\boldsymbol{X}, \boldsymbol{D}) = \delta^A_\alpha G_{AB}(\boldsymbol{X}, \boldsymbol{D})\delta^B_\beta = \delta^A_\alpha \bar{G}_{AB}(\boldsymbol{X})\hat{g}^\gamma_\beta(\boldsymbol{D})\delta^B_\gamma, \\ &\bar{g}_{\alpha\beta}(\boldsymbol{X}) = \delta^A_\alpha \bar{G}_{AB}(\boldsymbol{X})\delta^B_\beta; \end{aligned} \tag{2.49}$$

A local volume element $\mathrm{d}\tilde{v}$ and volume form $d\tilde{\omega}$ on the intermediate space are obtained, similarly to (2.32), as

$$\begin{aligned} &\mathrm{d}\tilde{v} = \{\det[(F^D)^a_A]\sqrt{\tilde{g}/G}\}\mathrm{d}V = J^D \mathrm{d}V, \\ &\mathrm{d}\tilde{v} = \{\det[(F^{E-1})^\alpha_a]\sqrt{\tilde{g}/g}\}\mathrm{d}v = j^E \mathrm{d}v; \\ &d\tilde{\omega} = J^D d\Omega = j^E d\omega. \end{aligned} \tag{2.50}$$

Jacobian determinants are defined for inelastic and thermoelastic mappings:

$$\begin{aligned} J^D &= \frac{1}{j^D} = \{\det[(F^D)^a_A]\sqrt{\tilde{g}/G}\} = \frac{\mathrm{d}\tilde{v}}{\mathrm{d}V}, \\ j^E &= \frac{1}{J^E} = \{\det[(F^{E-1})^\alpha_a]\sqrt{\tilde{g}/g}\} = \frac{\mathrm{d}\tilde{v}}{\mathrm{d}v}. \end{aligned} \tag{2.51}$$

For the convenient selection (2.49), $\tilde{g} = G$. The inelastic deformation $\boldsymbol{F}^D$ of (2.44) and (2.45), in indicial notation with basis vectors, is

$$\begin{aligned} \boldsymbol{F}^D[\boldsymbol{D}(\boldsymbol{X}, t)] &= (F^D)^\alpha_B[\boldsymbol{D}(\boldsymbol{X}, t)]\, \boldsymbol{g}_\alpha \otimes dX^B \\ &= (F^D)^A_B[\boldsymbol{D}(\boldsymbol{X}, t)] g^\alpha_A\, \boldsymbol{g}_\alpha \otimes dX^B, \end{aligned} \tag{2.52}$$

with $\boldsymbol{g}_\alpha$ generic basis vectors for the intermediate state and g^α_A shifter components from reference to intermediate configurations (Clayton 2014d). For consistency with (2.49),

$$\boldsymbol{g}_\alpha = \delta^A_\alpha \frac{\delta}{\delta X^A}; \qquad g^\alpha_A = \delta^\alpha_A, \quad \det(g^\alpha_A) = 1. \tag{2.53}$$

2.2 Balance equations and thermodynamics

General conservation laws for Finsler-continuum dynamics are developed in Sect. 2.2.1. Constitutive assumptions leading to thermodynamic identities follow in Sect. 2.2.2. Further derivations in the context of the multiplicative kinematic framework of Sect. 2.1.5 conclude the section in Sect. 2.2.3.

2.2.1 General conservation principles

Conservation laws for mass, momentum, and energy are derived in what follows next. This treatment extends the quasi-static variational approach of prior work (Clayton 2016b, 2017a, b) to the dynamic regime and reduces to the latter when the body is in static equilibrium.

Let m denote the mass of a material body, and dm a differential element of mass, where

$$\begin{aligned} \mathrm{d}m(\boldsymbol{X}) &= \rho_0(\boldsymbol{X}, \boldsymbol{D})\mathrm{d}V(\boldsymbol{X}, \boldsymbol{D}) \\ &= \rho[\boldsymbol{x}(\boldsymbol{X}, \boldsymbol{D}, t), \boldsymbol{D}, t]\mathrm{d}v[\boldsymbol{x}(\boldsymbol{X}, \boldsymbol{D}, t), \boldsymbol{D}, t]. \end{aligned} \tag{2.54}$$

Referential mass density ρ_0 is related to spatial mass density via application of (2.32):

$$\rho_0 = \rho J. \tag{2.55}$$

As in classical continuum mechanics in the absence of mass transport, ρ_0 is presumed constant in time at fixed point $\boldsymbol{X}$, though it may generally vary with $\boldsymbol{D}$. Therefore, its material time derivative vanishes, leading to a local mass balance upon use of (2.41):

$$\frac{D}{Dt}\rho_0 = 0 \Rightarrow \dot{\rho} + \rho v^a_{||a} = \frac{\partial \rho}{\partial t} + (\rho v)^a_{||a} = 0. \tag{2.56}$$

The rightmost equality can alternatively be derived by substituting $\phi = \rho$ into (2.43) and localizing the result, noting that the volume integral of spatial mass density over the current configuration of the body yields its total mass which is constant in time.

Let $n_a \mathrm{d}a$ and $N_A \mathrm{d}A$ denote area elements on the boundaries of $\mathfrak{m}$ and $\mathfrak{M}$, related by the usual Nanson's formula (Clayton 2014d) at a coincident point $\boldsymbol{x} = \boldsymbol{x}(\boldsymbol{X}, \boldsymbol{D}, t)$:

$$N_A \mathrm{d}A = j F^a_A n_a \mathrm{d}a. \tag{2.57}$$

Let $\mathrm{d}P^a = t^a \mathrm{d}a = t^a_0 \mathrm{d}A$ denote a component of a differential mechanical force vector, where traction components are defined according to

$$t^a = \sigma^{ab} n_b, \qquad t^a_0 = g^{ab} P^A_b N_A. \tag{2.58}$$

The first Piola-Kirchhoff stress P^A_a and Cauchy stress σ^{ab} are related by the deformation gradient and Jacobian determinant as follows from (2.58) and also obey a local angular momentum balance (Clayton 2016b, 2017a, b):

$$\sigma^{ab} = j g^{ac} P^A_c F^b_A = \sigma^{ba}. \tag{2.59}$$

In other words, Cauchy stress $\boldsymbol{\sigma}$ is symmetric. Let $\boldsymbol{B}$ denote a local body force vector measured per unit reference volume. The global balance of linear momentum is posited for material domain $\mathfrak{M}$ as

$$\frac{D}{Dt}\int_{\mathfrak{M}} \rho_0 \boldsymbol{v} \mathrm{d}V = \int_{\mathfrak{M}} \boldsymbol{B} \mathrm{d}V + \oint_{\partial\mathfrak{M}} \boldsymbol{t}_0 \mathrm{d}A. \tag{2.60}$$

Expressing the reference traction in terms of Piola-Kirchhoff stress via (2.58), using Stokes' theorem (2.14) for generalized pseudo-Finsler space, and localizing the result to a differential volume element at point $\boldsymbol{X}$ gives the following local balance of linear momentum:

$$\rho_0 \dot{v}^a = B^a + g^{ab} P^A_{b||A}. \tag{2.61}$$

Let U be the internal energy density measured per unit reference volume. Restricting the current presentation to adiabatic conditions, i.e., no heat flux or heat sources applied to the body, the global balance of energy is stated in integral form as

$$\begin{aligned} &\frac{D}{Dt}\int_{\mathfrak{M}} \left(\frac{\rho_0}{2}\boldsymbol{v}\cdot\boldsymbol{v} + U\right)\mathrm{d}V = \oint_{\partial\mathfrak{M}} \boldsymbol{t}_0 \cdot \boldsymbol{v} \mathrm{d}A \\ &+ \oint_{\partial\mathfrak{M}} \boldsymbol{z}\cdot\dot{\boldsymbol{D}}\mathrm{d}A + \int_{\mathfrak{M}} \boldsymbol{B}\cdot\boldsymbol{v}\mathrm{d}V, \end{aligned} \tag{2.62}$$

where $\boldsymbol{z}$ is a conjugate traction-like force to the time derivative of internal state defined by

$$\begin{aligned} &\dot{\boldsymbol{D}}(\boldsymbol{X}, t) = \frac{\partial D^A(\boldsymbol{X}, t)}{\partial t}\frac{\partial}{\partial D^A}, \\ &\boldsymbol{z} = z_A \delta D^A = Z^B_A N_B \delta D^A, \end{aligned} \tag{2.63}$$

with Z^B_A components of a corresponding stress-like tensor. The left side of (2.62) accounts for the rate of change of kinetic plus internal energy, the right side for work done by traction on the boundary and by the distributed body force. Use of (2.14), (2.58), (2.61), and (2.63) gives a global energy balance that can subsequently be localized to material point $\boldsymbol{X}$ as

$$\dot{U} = P^A_a v^a_{||A} + (Z^A_B \dot{D}^B)_{||A}. \tag{2.64}$$

The first term on the right is the stress power, the second the rate of working from changes in internal state. It is

again noted that when $\boldsymbol{D}$ is omitted from all equations, the resulting balances of mass, momentum, and energy reduce to their counterparts from nonlinear continuum mechanics (Clayton 2011) in Riemannian geometry (and more specifically, Euclidean space).

2.2.2 Constitutive assumptions and identities

Internal energy density per unit reference volume on $\mathfrak{M}$ is of the following general form:

$$U = U(\boldsymbol{F}, \eta, \boldsymbol{D}, \nabla \boldsymbol{D}, \boldsymbol{G}) = U(F^a_A, \eta, D^A, D^A_{|B}, G_{AB}). \tag{2.65}$$

Entropy density per unit reference volume is the scalar field $\eta(\boldsymbol{X}, \boldsymbol{D}, t)$. As discussed in Clayton (2016a), Clayton (2017a), physical reasoning behind this form follows from generalized continuum theories of materials with microstructure including phase field models (Capriz 1989; Clayton and Knap 2011a, 2015a; Levitas 2014). The internal state vector $\boldsymbol{D}$ is considered to be a vector-valued set of order parameter(s). Thermodynamic forces follow from the material time derivative and chain rule applied to (2.65):

$$\begin{aligned}\dot{U} &= \frac{\partial U}{\partial F^a_A}\dot{F}^a_A + \frac{\partial U}{\partial \eta}\dot{\eta} + \frac{\partial U}{\partial D^A}\dot{D}^A \\ &\quad + \frac{\partial U}{\partial D^A_{|B}}\frac{D}{Dt}(D^A_{|B}) + \frac{\partial U}{\partial G_{AB}}\dot{G}_{AB} \\ &= P^A_a \dot{F}^a_A + \theta\dot{\eta} + Q_A\dot{D}^A \\ &\quad + Z^B_A \frac{D}{Dt}(D^A_{|B}) + S^{AB}\dot{G}_{AB}.\end{aligned} \tag{2.66}$$

The temperature field is $\theta(\boldsymbol{X}, \boldsymbol{D}, t)$. Spatial coordinate invariance requires that strain dependence of internal energy density be of the form

$$\begin{aligned}U &= U[\boldsymbol{C}(\boldsymbol{F}, \boldsymbol{g}), \eta, \boldsymbol{D}, \nabla \boldsymbol{D}, \boldsymbol{G}] \\ &= U(C_{AB}, \eta, D^A, D^A_{|B}, G_{AB}).\end{aligned} \tag{2.67}$$

It follows that the first Piola-Kirchhoff stress P^A_a and Cauchy stress σ^{ab} obey a local angular momentum balance that agrees with (2.59):

$$\begin{aligned}P^A_a &= 2g_{ab}F^b_B\frac{\partial U}{\partial C_{AB}}, \\ \sigma^{ab} &= jg^{ac}P^A_c F^b_A = 2jF^a_A F^b_B\frac{\partial U}{\partial C_{AB}} = \sigma^{ba}.\end{aligned} \tag{2.68}$$

Invoking a variational principle in prior work (Clayton 2017a), a local equilibrium equation was derived for micro-momentum, containing terms in $\boldsymbol{Q}$ and $\boldsymbol{Z}$. In the dynamic regime, a rate equation for internal state vector components D^A is posited by setting the residual of that equilibrium equation proportional to the negative rate of internal state:

$$\begin{aligned}\dot{D}^K = -\mathsf{L}^{KC}[&Q_C - \partial_A Z^A_C - Z^B_C H^A_{AB} + Z^A_B H^B_{AC} \\ &- \bar{\partial}_B Z^A_C \partial_A D^B - Z^B_A(\bar{\partial}_C N^A_B \\ &- \bar{\partial}_C K^A_{BD} D^D + \delta^A_C C^D_{ED} D^E_{;B}) \\ &- P^A_a \bar{\partial}_B \bar{\partial}_C \varphi^a \partial_A D^B \\ &+ (S^{AB} + UG^{AB})\bar{\partial}_C G_{AB}].\end{aligned} \tag{2.69}$$

Here, L^{KC} is a positive definite matrix of constants (depending on the material) that control the time scale for the rate of change of internal state. Equation (2.69) states that the order parameters evolve in time such that at equilibrium, the term in square braces vanishes in accordance with the static director momentum equation derived previously (Clayton 2017a). Kinetic equation (2.69) can be expressed in condensed form as

$$\dot{D}^K = -\mathsf{L}^{KC}\left[\frac{\partial U}{\partial D^C} - \nabla_A\left(\frac{\partial U}{\partial \nabla_A D^C}\right) + \cdots\right], \tag{2.70}$$

where here ∇ is the horizontal covariant derivative and remaining terms have been truncated only for presentation purposes. This equation is reminiscent of the time dependent Ginzburg-Landau or Allen-Cahn equations (Allen and Cahn 1979; Levitas 2014).

Several choices depending on the class of material complete the model. A metric tensor $\boldsymbol{G}$ is introduced, from which connection coefficients are obtained from relations in Sect. 2.1.1. Horizontal and vertical connection coefficients in (2.8) and (2.9) must be chosen, typically those of the Chern-Rund connection. Similar features are assigned for the current configuration, as described by equations of Sect. 2.1.2. The internal energy density function U in (2.65) must be assigned. Finally, constitutive equations for inelastic components of the deformation gradient, $\boldsymbol{F}^D$ of Sect. 2.1.5, are usually needed, as are kinetic coefficients L^{KC} for general dynamic problems.

2.2.3 Multiplicative thermodynamics

Extending prior treatments of Clayton (2016a, 2017a, b) to account for entropy, and those addressed in phase

field theory (Clayton and Knap 2011a, 2015a), the internal energy U of (2.65) is split into a sum of thermoelastic energy density W and structure/internal state dependent energy density f:

$$U(F^a_A, \eta, D^A, D^A_{|B}, G_{AB}) = W[(F^E)^a_\alpha, \eta, D^A, \bar{g}_{\alpha\beta}] + f(D^A, D^A_{|B}, \bar{G}_{AB}). \tag{2.71}$$

Notice that general dependence on $\boldsymbol{F}$ is replaced by dependence on its thermoelastic part $\boldsymbol{F}^E$. A more general treatment would allow for couplings among elastic deformation, entropy, and internal state. For terms entering the multiplicative kinematics, the conditions (2.44) and (2.45) are imposed:

$$(F^E)^a_\alpha[\boldsymbol{F}, \boldsymbol{F}^D(\boldsymbol{D})] = F^a_A[\boldsymbol{X}, \boldsymbol{D}(\boldsymbol{X}, t), t](F^{D\,-1})^A_\alpha[\boldsymbol{D}(\boldsymbol{X}, t)]. \tag{2.72}$$

Applying (2.72) and invoking (2.49) for intermediate space metric components $\bar{g}_{\alpha\beta}$, thermodynamic forces of (2.66), at fixed $\boldsymbol{X}$, obey

$$\begin{aligned} P^A_a &= \frac{\partial U}{\partial F^a_A} = \frac{\partial W}{\partial F^a_A} = (F^{D\,-1})^A_\alpha \frac{\partial W}{\partial (F^E)^a_\alpha}, \\ \theta &= \frac{\partial U}{\partial \eta} = \frac{\partial W}{\partial \eta}; \\ Q_A &= \frac{\partial U}{\partial D^A} = \frac{\partial W}{\partial D^A} + \frac{\partial f}{\partial D^A} - P^B_a (F^E)^a_\alpha \frac{\partial (F^D)^\alpha_B}{\partial D^A}, \\ Z^B_A &= \frac{\partial U}{\partial D^A_{|B}} = \frac{\partial f}{\partial D^A_{|B}}. \end{aligned} \tag{2.73}$$

Furthermore, $\partial U/\partial G_{AB} \to \partial U/\partial \bar{G}_{AB}$ and $\dot{\bar{G}}_{AB}(\boldsymbol{X}) = 0$, so $S^{AB} \to 0$ in (2.66) and (2.69) without energetic consequence. Spatial invariance analogous to (2.67) follows from forcing W to depend on $\boldsymbol{C}^E$ rather than $\boldsymbol{F}^E$, where

$$\begin{aligned} (C^E)_{\alpha\beta} &= (F^E)^a_\alpha \bar{g}_{ab} (F^E)^b_\beta = (F^{D\,-1})^A_\alpha \bar{C}_{AB} (F^{D\,-1})^B_\beta, \\ \bar{C}_{AB} &= F^a_A \bar{g}_{ab} F^b_B. \end{aligned} \tag{2.74}$$

3 Theory: moving surfaces of discontinuity

Consider a planar shock moving with a normal component of natural velocity D in the material manifold $\mathfrak{M}$, across which velocity, stress, and deformation gradient may be discontinuous. Let $(\cdot)^+$ and $(\cdot)^-$ denote values of a quantity upstream and downstream from the shock. The jump of a quantity across the shock plane is then

$$[\![\cdot]\!] = (\cdot)^- - (\cdot)^+. \tag{3.1}$$

Denote by $\mathsf{w} = \mathsf{v} - \mathsf{D}$ the velocity of the material relative to the shock front, with v the scalar particle velocity, i.e., the component of velocity vector $\boldsymbol{\upsilon}$ parallel to the direction of shock propagation. For convenience, let the shock direction be parallel to X^1, and further assume that uniaxial strain conditions hold:

$$\boldsymbol{F} = \boldsymbol{1} + (\partial u/\partial X)\boldsymbol{g}_1 \otimes \boldsymbol{G}^1. \tag{3.2}$$

Basis vectors $\boldsymbol{g}_1$ and $\boldsymbol{G}^1$ point in the direction of motion $X = X^1$, and $u(\boldsymbol{X}, \boldsymbol{D}, t)$ is the displacement component in this direction. The equal first Piola-Kirchhoff and Cauchy stress components normal to the front are equal to the negative of the so-called shock pressure, i.e., $P^1_1 = \sigma^1_1 = -P$. The internal energy per unit mass is $e = U/\rho_0$.

The form of Reynolds' transport theorem derived in (2.43) can be used in conjunction with assumptions and definitions for time derivatives in Sect. 2.1.4 to obtain a general transport theorem accounting for flux of a quantity $\phi(\boldsymbol{x}, \boldsymbol{D}, t)$ across the shock plane. The derivations of Casey (Casey 2011) (in Euclidean space) apply in full when the above definitions and caveats for Finsler space hold. Specifically, let subscripts 1 and 2 denote subregions of the body manifold $\mathfrak{M}$ partitioned by a shock plane $\Sigma(t)$. Then the transport theorem can be expressed as (Casey 2011)

$$\dot{\Phi} = \frac{D}{Dt}\int_{\mathfrak{m}} \phi \mathrm{d}v = \dot{\Phi}_1 + \dot{\Phi}_2 + \int_\Sigma [\![\phi \mathsf{w}]\!] \mathrm{d}a. \tag{3.3}$$

The first two terms following the second equality account for rates of change of ϕ in each subregion. First taking $\phi = \rho$ in (3.3), the global form of mass conservation law (2.56) requires that $\dot{\Phi}$ vanish for each subregion as well as for the whole body, leaving

$$[\![\rho \mathsf{w}]\!] = 0. \tag{3.4}$$

Next taking $\phi = \rho \mathsf{v}$ as the spatial linear momentum, conservation law (2.60) requires

$$[\![P + \rho \mathsf{v}\mathsf{w}]\!] = 0. \tag{3.5}$$

Let $\boldsymbol{\zeta}$ denote the Piola transform of $\boldsymbol{z}$ in (2.62):

$$\zeta_A \mathrm{d}a = Z^a_A n_a \mathrm{d}a = j F^a_B Z^B_A n_a \mathrm{d}a = Z^B_A N_B \mathrm{d}A = z_A \mathrm{d}A. \tag{3.6}$$

Then the conservation law for energy is obtained by setting $\phi = \rho(e + \frac{1}{2}\mathsf{v}^2)$ in (3.3) and using (2.62) and (3.6):

$$[\![\rho \mathsf{w}(e + \mathsf{v}^2/2) + P\mathsf{v} - \boldsymbol{\zeta} \cdot \dot{\boldsymbol{D}}]\!] = 0. \tag{3.7}$$

Equations (3.4) and (3.5) are identical in form to the classical Rankine-Hugoniot conditions, while (3.7) reduces to its classical counterpart when $\boldsymbol{\zeta} \cdot \dot{\boldsymbol{D}} = 0$.

The equations simplify further when the material is undeformed, unstressed, and at rest ahead of the shock, with null internal energy ($U^+ = 0$) taken as the datum. In that case, algebraic manipulations yield

$$\mathsf{v} = -\mathsf{D}\frac{\partial u}{\partial X}, \qquad P = \rho_0 \mathsf{v}\mathsf{D},$$
$$U = \frac{1}{2}\rho_0 \mathsf{v}^2 - \frac{1}{\mathsf{D}}[\![\boldsymbol{\zeta} \cdot \dot{\boldsymbol{D}}]\!]. \tag{3.8}$$

Quantities in each equality correspond to the downstream (shocked) state besides the jump term on the right side of final equation in (3.8). The latter term, written in general vector form for the moment, is subjected to further assumptions later upon specification of a particular constitutive model.

4 Application: shock loading of boron carbide

The dynamic theory of Finsler-geometric continuum mechanics is now applied to shock loading of ceramic single crystals. In particular, the problem considered in Sect. 4 is focused on anisotropic boron carbide (B_4C) subjected to planar impact loading along its c-axis ([0001]). The pseudo-Finsler metric quantifies local densification (i.e., local volume decrease) that accompanies the stress-induced phase transformation from a trigonal crystal to glassy phase (Yan et al. 2009; Clayton 2012a, 2013a, 2014a; Clayton and Tonge 2015; Taylor et al. 2012; Taylor 2015; An and Goddard 2015a). Inelasticity arises from two contributions: the aforementioned volume change and shear strain within amorphous bands (Chen et al. 2003; An and Goddard 2015a). The boundary value problem involves steady shock wave propagation, under conditions of uniaxial strain compression, of a nonlinear elastic domain of the ceramic. The presentation that follows proceeds from a general constitutive description to a focused solution of the specific problem.

4.1 Geometry and deformation

The material body is a domain of effectively infinite dimensions. Uniaxial strain conditions are imposed, with compression in the X^3-direction. The internal state vector is prescribed as $\{D^A\} \to \{0, 0, D^3\}$, later linked physically to structure collapse of boron carbide. By construction, field variables may vary only with $Z = X^3$ and $D = D^3$. Components D^1 and D^2 are superfluous, while X^1 and X^2 are important in the context of lateral, i.e., transverse, stresses, for example. A Cartesian coordinate system is used for $\{X^A\}$, and thus the metric tensor $\boldsymbol{G}$ contains no explicit dependence on $\boldsymbol{X}$.

Definitions and identities of Sect. 2.1 are given more specific forms to be consistent with these protocols. An isotropic metric tensor is prescribed, similar to that in prior work (Clayton 2016b):

$$\{X, Y, Z\} = \{X^1, X^2, X^3\}, \qquad D = D^3 = D(Z, t); \tag{4.1}$$

$$\boldsymbol{G}(D) = \hat{\boldsymbol{G}}(D) = B(D)\mathbf{1} = \begin{bmatrix} B(D) & 0 & 0 \\ 0 & B(D) & 0 \\ 0 & 0 & B(D) \end{bmatrix},$$

$$G_{AB} = B\delta_{AB}; \qquad G = \det \boldsymbol{G} = B^3(D); \tag{4.2}$$

$$\gamma_{ABC} = \tfrac{1}{2}(\partial_A G_{BC} + \partial_B G_{AC} - \partial_C G_{AB}) = 0,$$
$$G^A = \tfrac{1}{2}\gamma^A_{BC} D^B D^C = 0, \quad N^A_B = \bar{\partial}_B G^A = 0$$
$$\Rightarrow \delta_A(\cdot) = \partial_A(\cdot); \tag{4.3}$$

$$C_{131} = C_{311} = C_{333} = C_{322} = C_{232} = B'/2,$$
$$C_{113} = C_{223} = -B'/2. \tag{4.4}$$

The prime notation obeys $B'(D) = \mathrm{d}B(D)/\mathrm{d}D$, and all other covariant components C_{ABC} of Cartan's tensor are zero. The Cartesian metric $\mathbf{1}$ is scaled isotropically by scalar function B, a conformal transformation of Weyl type (Weyl 1952; Clayton 2016a, 2017a). The pseudo-Finsler manifold $\mathfrak{M}$ is locally Minkowskian Minguzzi (2014).

Components of coefficients of the Chern-Rund connection are used, also following prior work (Clayton 2016b, 2017a). From this choice and from the vanishing nonlinear connection coefficients in (4.3), it follows that

$$H^A_{BC} = K^A_{BC} = \Gamma^A_{BC} = \tfrac{1}{2}G^{AD}(\delta_C G_{BD} + \delta_B G_{CD} - \delta_D G_{BC}) = 0;$$
$$V^A_{BC} = Y^A_{BC} = 0. \tag{4.5}$$

For the spatial configuration, i.e., the deformed material manifold $\mathfrak{m}$, coordinates and metric tensor are of fully analogous forms to those used for $\mathfrak{M}$. Invoking lower case font for the spatial frame,

$$\{x, y, z\} = \{x^1, x^2, x^3\}, \quad d = d^3 = d(z, t);$$
$$\boldsymbol{g}(d) = \hat{\boldsymbol{g}}(d) = b(d)\mathbf{1}, \quad g_{ab} = b\delta_{ab},$$
$$g(d) = b^3(d); \tag{4.6}$$
$$\gamma_{abc} = \tfrac{1}{2}(\partial_a g_{bc} + \partial_b g_{ac} - \partial_c g_{ab}) = 0,$$
$$g^a = \tfrac{1}{2}\gamma^a_{bc} d^b d^c = 0,$$
$$n^a_b = \bar{\partial}_b g^a = 0 \Rightarrow \delta_a(\cdot) = \partial_a(\cdot); \tag{4.7}$$
$$C_{131} = C_{311} = C_{333} = C_{322} = C_{232} = b'/2,$$
$$C_{113} = C_{223} = -b'/2, \tag{4.8}$$

where $b'(d) = \mathrm{d}b(d)/\mathrm{d}d$. The spatial geometry is also locally Minkowskian. Using Chern-Rund connection coefficients with vanishing nonlinear coefficients from (4.7),

$$H^a_{bc} = K^a_{bc} = \Gamma^a_{bc} = \tfrac{1}{2}g^{ad}(\delta_c g_{bd} + \delta_b g_{cd} - \delta_d g_{bc}) = 0;$$
$$V^a_{bc} = Y^a_{bc} = 0. \tag{4.9}$$

Summarizing, nonlinear connection coefficients (N^A_B and n^a_b) vanish identically in both configurations, as do Chern-Rund coefficients (Γ^A_{BC} and Γ^a_{bc}). Cartan's coefficients C^A_{BC} and C^a_{bc} may be nonzero. The horizontal covariant derivatives of the metric tensors vanish so $(\sqrt{G})_{|A} = 0$ and $(\sqrt{g})_{|a} = 0$. Thus, use of Rund's version of Stokes' theorem of (2.14), (2.15), and (2.25) to derive balance and transport equations is mathematically valid. Vertical connection coefficients (V^A_{BC},V^a_{bc},Y^A_{BC}, and Y^a_{bc}) all vanish by definition, which greatly simplifies calculations.

Motions, deformations, and director gradients defined in Sect. 2.1.3 take the following forms under unaxial strain conditions. Let $z = \varphi(Z, D, t)$ denote deformation in the Z direction with $\epsilon(Z, D, t)$ a corresponding displacement gradient measure, negative in compression, such that

$$x = X, \quad y = Y, \quad z = \varphi;$$
$$d = d(Z, D, t); \qquad D = D(Z, t); \tag{4.10}$$

$$\boldsymbol{F}(X, D, t) = \begin{bmatrix} \partial x(X)/\partial X & \partial x(X)/\partial Y & \partial x(X)/\partial Z \\ \partial y(Y)/\partial X & \partial y(Y)/\partial Y & \partial y(Y)/\partial Z \\ \partial\varphi(Z, D, t)/\partial X & \partial\varphi(Z, D, t)/\partial Y & \partial\varphi(Z, D, t)/\partial Z \end{bmatrix}$$
$$= \begin{bmatrix} 1 & 0 & 0 \\ 0 & 1 & 0 \\ 0 & 0 & \partial\varphi(Z, D, t)/\partial Z \end{bmatrix} = \begin{bmatrix} 1 & 0 & 0 \\ 0 & 1 & 0 \\ 0 & 0 & 1 + \epsilon(Z, D, t) \end{bmatrix}; \tag{4.11}$$

$$J = F^1_1 F^2_2 F^3_3 \sqrt{g/G} = F^3_3 (g/G)^{1/2} = (1 + \epsilon)(b/B)^{3/2}; \tag{4.12}$$
$$D^3_{|3} = \partial_3 D - N^3_3 + K^3_{33} D = \partial D/\partial Z = D', \tag{4.13}$$

where the prime notation in (4.13) denotes a partial derivative with respect to the axial coordinate.

The non-vanishing component of the director vector, i.e., the internal state variable D, is physically related to transformation to a glassy phase and shear failure of boron carbide. An overall loss of shear strength and volume collapse are simultaneously associated with nonzero values of D. A regularization constant l with dimensions of length and a normalized order parameter $\xi \in [0, 1]$ are now introduced:

$$\xi = D/l, \qquad \xi' = D'/l. \tag{4.14}$$

The scalar l is identified as the value of state variable D at which the material ruptures and undergoes complete densification, and it is assumed to be a material property. Letting k denote a constant depending on the material, a more specific form of the pseudo-Finsler material metric in (4.2) is now prescribed:

$$\boldsymbol{G}(D) = B(D)\mathbf{1} = \exp[(k/3)(D/l)^2]\mathbf{1};$$
$$G(\xi) = B^3(\xi) = \exp(k\xi^2)$$
$$\Rightarrow 3B'/(2B) = kD/l = k\xi. \tag{4.15}$$

The third/axial component of the trace of Cartan's tensor of (4.4) will be used later:

$$C^A_{3A} = G^{AB}C_{3AB} = G^{11}C_{311} + G^{22}C_{322} + G^{33}C_{333} = 3B'/(2B) = kD/l = k\xi. \tag{4.16}$$

This form of conformal transformation is similar, but not identical, to that used in Clayton (2017a). A benefit of the current prescription is vanishing of (4.16) at $\xi = 0$, which eliminates certain driving force contributions for transformation in the fully elastic state. The length of a referential line element in (2.10) and the corresponding volume form in (2.11) become

$$|\mathrm{d}\boldsymbol{X}|^2 = \exp[(k/3)(D/l)^2](\mathrm{d}X \cdot \mathrm{d}X + \mathrm{d}Y \cdot \mathrm{d}Y + \mathrm{d}Z \cdot \mathrm{d}Z),$$
$$d\Omega = \exp[(k/2)(D/l)^2]\mathrm{d}X \wedge \mathrm{d}Y \wedge \mathrm{d}Z. \tag{4.17}$$

For $\xi > 0$, expansion occurs when $k > 0$ and contraction when $k < 0$. Volume collapse in boron carbide is associated with the latter condition.

As in prior work (Clayton 2016b, 2017a, b), the spatial and referential state vector entries are set to coincide in the sense (4.10):

$$d(Z, D, t) = D(Z, t) = l\xi(Z, t). \tag{4.18}$$

This can be interpreted as a scalar push-forward relation for field D (Clayton 2017b). An analogous Weyl-type form of the spatial metric of (4.6) is

$$\boldsymbol{g}(d) = b(d)\mathbf{1} = \exp[(k/3)(D/l)^2]\mathbf{1};$$
$$g(\xi) = b^3(\xi) = \exp(k\xi^2) \Rightarrow 3b'/(2b) = kD/l = k\xi. \tag{4.19}$$

With these choices of metrics, (4.12) reduces to

$$J(Z, D, t) = F_3^3(Z, D, t) = 1 + \epsilon(Z, D, t). \tag{4.20}$$

As remarked already, inelasticity in shock compressed boron carbide consists of contributions of densification as well as shearing in amorphous bands. For compressive loading normal to the c-axis, densification is presumed spherical as in Clayton (2016b). Also, for loading according to this protocol, inelastic shearing takes place on planes and in directions analogous to those for pyramidal slip of the type $\langle\bar{1}101\rangle\{01\bar{1}\bar{1}\}$ in hexagonal crystals, following examination of recovered fragments (Chen et al. 2003; Yan et al. 2009). Shear localization and amorphization for this kind of deformation system were studied via atomic simulations of simple shearing of boron carbide single crystals in An and Goddard (2015a), wherein no twinning or dislocation glide were reported. These authors further considered shearing of a different crystal orientation $\langle 10\bar{1}0\rangle\{0001\}$ resulting in twinning and amorphization on the basal plane. The present study does not address basal plane localization or twinning since elastic driving forces (i.e., resolved shear stress) on (0001) vanish and since such modes are inconsistent with symmetry for c-axis compression of the crystal.

The multiplicative description of (2.44) is used, with the inelastic portion containing microstructure (i.e., D) dependent terms. The total deformation gradient in Cartesian coordinates is

$$\boldsymbol{F} = \begin{bmatrix} 1 & 0 & 0 \\ 0 & 1 & 0 \\ 0 & 0 & 1+\epsilon \end{bmatrix} = \boldsymbol{F}^E\boldsymbol{F}^D = \begin{bmatrix} (F^E)^x_X & 0 & 0 \\ 0 & (F^E)^y_Y & 0 \\ 0 & 0 & (F^E)^z_Z \end{bmatrix} \begin{bmatrix} (F^D)^X_X & 0 & 0 \\ 0 & (F^D)^Y_Y & 0 \\ 0 & 0 & (F^D)^Z_Z \end{bmatrix}. \tag{4.21}$$

The inelastic term is diagonal due to symmetry of the crystal structure and the present loading mode. It accounts for the inelastic volume change β and inelastic shearing γ_0 on the six pyramidal systems of type $\langle\bar{1}101\rangle\{01\bar{1}\bar{1}\}$:

$$\boldsymbol{F}^D(\xi) = \mathbf{1} + \iota(\xi)\left[\chi\mathbf{1} + \gamma_0\sum_{\alpha=1}^{6}\boldsymbol{s}^\alpha \otimes \boldsymbol{m}^\alpha + \frac{\gamma_0^2}{2}\left(\sum_{\alpha=1}^{6}\boldsymbol{s}^\alpha \otimes \boldsymbol{m}^\alpha\right)^2 + \frac{\gamma_0^3}{6}\left(\sum_{\alpha=1}^{6}\boldsymbol{s}^\alpha \otimes \boldsymbol{m}^\alpha\right)^3\right]. \tag{4.22}$$

Here, the material constant $\chi = \frac{1}{3}[\exp(k/2) - 1]$ accounts for isotropic volume collapse with $k < 0$. Unit vectors $\boldsymbol{s}^\alpha$ and $\boldsymbol{m}^\alpha$ are the orthogonal direction and plane for inelastic pyramidal shear of maximum magnitude γ_0, another material constant. The terms containing γ_0 are the first three in the series approximation of the exponential function corresponding to an exact representation of this symmetric inelastic deformation mode (Clayton 2014b, e). Finally, $\iota(\xi) : [0, 1] \rightarrow [0, 1]$ is an interpolation function with vanishing endpoint derivatives, specifically as used in phase field representations of structural changes (Levitas et al. 2009; Clayton and Knap 2011a):

$$\iota(\xi) = 3\xi^2 - 2\xi^3, \qquad \iota'(\xi) = 6\xi(1-\xi). \tag{4.23}$$

The form of (4.22) scales contributions of phase transformation and inelastic shearing by a phase field-type of interpolation function (4.23). The first term in square braces is assumed isotropic or spherical, accounting for compaction commensurate with the crystal-to-glass transition. Depending on the loading protocol and deformation system, the phase change could demonstrate some anisotropy (e.g., preferential structure collapse along the c-axis (Yan et al. 2009; Clayton 2012a)), but the present work, as in Clayton (2016b), simplifies this part of transformation strain as isotropic. Terms involving the dyadic product of shearing direction and plane encompass all deviatoric mechanisms associated with amorphization, shear localization, and eventual mode II failure on pyramidal planes. The assumption that evolution of volumetric and deviatoric inelastic deformations proceed in lock-step, via the same function ι, benefits from simplicity and is demonstrated later to depict physically reasonable solutions to the present highly symmetric, one-dimensional shock problem for compressive strains up to on the order of 20%. Generalizations, albeit at the possible expense of further assumptions or calibration, are anticipated to be necessary in the future to address more sophisticated problems.

Noting that slip/shear is isochoric, the inelastic volume change is approximately

$$J^D = \det \boldsymbol{F}^D \approx (1+\iota\chi)^3 \approx 1 + 3\iota\chi = \iota \exp(k/2). \tag{4.24}$$

Crystal plasticity-type representations of inelastic shearing modes distinct from slip have been used elsewhere for cleavage fracture in rocks (Clayton 2010) and other brittle solids (Aslan et al. 2011).

Parameter γ_0 is regarded as a constant for simplicity, here describing shearing on pyramidal planes. For other deformation systems or other shear mechanisms in boron carbide, γ_0 would presumably vary, and it would also presumably vary with material composition. In (4.22), function $\iota(\xi)$ scales the magnitude of shear deformation, where evolution of ξ is dictated by a kinetic process or incremental equilibrium conditions.

The material logarithmic thermoelastic strain tensor $\boldsymbol{e}^E$ is used in the constitutive model of boron carbide, as in Clayton and Tonge (2015), Clayton (2017b). This strain tensor more accurately represents the nonlinear elastic response of strong solids with a large ratio of effective shear to bulk modulus such as quartz (Clayton 2014b, 2015c) and boron carbide (Clayton and Tonge 2015) than the Green elastic strain (Clayton and McDowell 2003; Clayton 2011) or Eulerian material strain (Clayton 2013b; Lloyd et al. 2014b). The logarithm of the elastic stretch corresponding to the first of (2.74) is

$$\boldsymbol{e}^E = \ln \boldsymbol{U}^E = \ln[(\boldsymbol{C}^E)^{1/2}] = \frac{1}{2}\ln \boldsymbol{C}^E,$$
$$(e^E)^\alpha_\beta = \frac{1}{2}(\ln C^E)^\alpha_\beta. \tag{4.25}$$

For the present class of problems with (4.11) and (4.21) now invoked and $\bar{g}_{\alpha\beta} = \delta_{\alpha\beta}$, the first of (2.74) results in the following three possibly nonzero components:

$$(C^E)^1_1 = [(F^E)^x_X]^2, \qquad (C^E)^2_2 = [(F^E)^y_Y]^2,$$
$$(C^E)^3_3 = [(F^E)^z_Z]^2. \tag{4.26}$$

Computation of the thermoelastic logarithmic strain (omitting the redundant numerical superscript) is then trivial since $\boldsymbol{C}^E$ is diagonal:

$$e^E_1 = (e^E)^X_X = \ln[(F^E)^x_X],$$
$$e^E_2 = (e^E)^Y_Y = \ln[(F^E)^y_Y],$$
$$e^E_3 = (e^E)^Z_Z = \ln[(F^E)^z_Z]. \tag{4.27}$$

Thermoelastic volume change is related to the trace of the logarithmic strain via $\ln J^E = e^E_1 + e^E_2 + e^E_3$.

4.2 Thermomechanics

The internal energy per unit reference volume U in (2.65) is additively split into a thermoelastic strain energy per unit reference volume W and a structure or phase dependent energy per unit reference volume f, following (2.71). The following sum is used:

$$U(F^a_A, \eta, D^A, D^A_{|B}, G_{AB}) = W(e^E_{\alpha\beta}, \eta) + f(D^A, D^A_{|B}); \tag{4.28}$$

$$W = \frac{1}{2}C^{\alpha\beta\gamma\delta}e^E_{\alpha\beta}e^E_{\gamma\delta} + \frac{1}{6}C^{\alpha\beta\gamma\delta\epsilon\phi}e^E_{\alpha\beta}e^E_{\gamma\delta}e^E_{\epsilon\phi} + \theta_0\eta[1 - \Gamma^{\alpha\beta}_0 e^E_{\alpha\beta} + \eta/(2c_0)]; \tag{4.29}$$

$$f = \frac{\Upsilon}{l}|\nabla \boldsymbol{D}|^2 + \frac{\Upsilon}{l^3}|\boldsymbol{D}|^2 + A\left(\frac{|\boldsymbol{D}|}{l}\right)^2\left(1 - \frac{|\boldsymbol{D}|}{l}\right)^2. \tag{4.30}$$

The thermoelastic strain energy function W is essentially identical to one used in Clayton and Tonge (2015),

accounting for anisotropic linear and nonlinear elastic effects, thermoelastic coupling, and specific heat. Entropy $\eta = 0$ and temperature $\theta = \theta_0$ for the datum of the ambient reference state. Isentropic second- and third-order elastic constants are $C^{\alpha\beta\gamma\delta}$ and $C^{\alpha\beta\gamma\delta\epsilon\phi}$. These are taken herein to be independent the phase of the solid since inelastic deformation rather than moduli degradation as in Clayton (2016b) now accounts for shear softening. The specific heat at constant elastic strain per unit reference volume is the constant c_0. The anisotropic and symmetric Grüneisen tensor most generally consists of six constants $\Gamma_0^{\alpha\beta}$. Since $G_{AB}(\boldsymbol{D}) = \delta_{AB} B(\boldsymbol{D})$, explicit dependence of functions on the right side of (4.28) on the metric tensor would be redundant.

The microstructure dependent function f consists of three parts: a form quadratic in $|\boldsymbol{D}|$, representative of fracture or rupture; a form quadratic in $|\nabla \boldsymbol{D}|$, accounting for energy of phase boundaries, shear bands, and/or crack surfaces; and a double well potential of order four in $|\boldsymbol{D}|$. The surface energy per unit reference area is the intrinsic material constant Υ. This energy can be associated with the formation of mode II shear zones commensurate with cavitation and rupture upon complete amorphization (An and Goddard 2015a). The first term on the right side of (4.30) is the standard quadratic form for gradients of order parameter(s) in models of fracture (Clayton and Knap 2014, 2015b) and phase transformations, e.g., Levitas (2014). The second term on the right side of (4.30) is the usual prescription for bulk fracture energy in phase field theory (Clayton and Knap 2014, 2015a). Finally, the double well potential with barrier strength quantified by A, a constant of dimensions of energy per unit reference volume, is the conventional form used in phase field models of phase transformations and twinning (Clayton and Knap 2011a; Levitas 2014). In the present work, the phase transformation corresponding to the double well potential is that from crystal to amorphous solid in B_4C. In summary, f is a hybrid potential combining standard forms from the literature to account for energies associated with related processes of phase transformation, shear localization, and shear failure in shock loaded boron carbide crystals.

The generic energy densities W and f are applicable to any loading direction and any Cartesian coordinate system, with full anisotropy and a vector-valued internal state variable, respectively. These general forms are simplified further for the present application in shock physics with an effectively scalar order parameter. Regarding thermoelastic strain energy, the Grüneisen scalar is used for thermoelastic coupling, and an isotropic contribution from third-order elasticity is used to account for increases in tangent bulk modulus with increasing mass density under shock compression. Letting B_0 and B_0' denote the isentropic bulk modulus and its pressure derivative at the reference state, and letting $\Gamma_0^{\alpha\beta} \rightarrow \Gamma_0 \delta^{\alpha\beta}$, the strain energy function in (4.29) becomes

$$W = \frac{1}{2}\mathsf{C}_{IJ} e_I^E e_J^E + \frac{1}{6} B_0 (2 - B_0')(\ln J^E)^3 + \theta_0 \eta [1 - \Gamma_0 \ln J^E + \eta/(2c_0)]. \tag{4.31}$$

Indices $I, J = 1, 2, \ldots 6$ denote Voigt notation, and C_{IJ} are the second-order elastic constants to be introduced for boron carbide in Sect. 4.3. Now considering (4.13) and (4.14) whereby $D(Z,t) = l\xi(Z,t)$ is the only relevant component of $\boldsymbol{D}$, the phase transition and fracture energy function in (4.30) becomes

$$f = \Upsilon l [\xi^2/l^2 + (\xi')^2] + A\xi^2(1-\xi)^2. \tag{4.32}$$

More specific forms of thermodynamic forces for Finsler continuum mechanics at a fixed material point $\boldsymbol{X}$ are then obtained:

$$P_a^A = \frac{\partial U}{\partial F_A^a} = (F^{D\,-1})_\alpha^A \frac{\partial W}{\partial (F^E)_\alpha^a} = (F^{D\,-1})_\alpha^A \frac{\partial W}{\partial e_{\gamma\beta}^E} \frac{\partial e_{\gamma\beta}^E}{\partial (F^E)_\alpha^a}, \tag{4.33}$$

$$\theta = \frac{\partial U}{\partial \eta} = \frac{\partial W}{\partial \eta} = \theta_0 \left(1 - \Gamma_0 \ln J^E + \frac{\eta}{c_0}\right), \tag{4.34}$$

$$\begin{aligned} Q = Q_3 = Q_Z &= \frac{\partial U}{\partial D} \\ &= \frac{1}{l}\left[\frac{\partial f}{\partial \xi} - P_a^A (F^E)_\alpha^a \frac{\partial (F^D)_A^\alpha}{\partial \xi}\right] \\ &= \frac{1}{l}\left[2\frac{\Upsilon}{l}\xi + 2A\xi(1-\xi)(1-2\xi) - P_a^A (F^E)_\alpha^a \frac{\partial (F^D)_A^\alpha}{\partial \xi}\right], \end{aligned} \tag{4.35}$$

$$T = Z_Z^Z = Z_3^3 = \frac{\partial U}{\partial D_{|3}} = \frac{1}{l}\frac{\partial f}{\partial \xi'} = 2\Upsilon \xi'. \tag{4.36}$$

For the present problem of shock compression, now consider the Cartesian coordinate system and uniaxial strain conditions of Sect. 4.1. Boron carbide single crystals have rhombohedral, i.e., trigonal symmetry.

The current application assigns the XY-plane as the basal plane, i.e., (0001) in hexagonal Miller-Bravais indices, with Z the direction of loading along [0001]. For this loading mode, pertinent isentropic second-order elastic constants in Voigt notation are $\mathsf{C}_{11} = \mathsf{C}_{22}$, C_{33}, C_{12}, and $\mathsf{C}_{13} = \mathsf{C}_{23}$. Other loading directions or more general crystal orientations might require use of $\mathsf{C}_{14} = -\mathsf{C}_{24} = \mathsf{C}_{56}$ which are not needed here. The thermoelastic strain energy in (4.29) and (4.31) becomes, for the potentially nonzero elastic strain components in (4.27),

$$\begin{aligned} W = W(e_1^E, e_2^E, e_3^E, \eta) &= \frac{1}{2}[\mathsf{C}_{11}(e_1^E)^2 + \mathsf{C}_{11}(e_2^E)^2 \\ &+ \mathsf{C}_{33}(e_3^E)^2 + 2(\mathsf{C}_{12}e_1^E e_2^E \\ &+ \mathsf{C}_{13}e_1^E e_3^E + \mathsf{C}_{13}e_2^E e_3^E)] \\ &+ \frac{1}{6}B_0(2 - B_0')(e_1^E + e_2^E + e_3^E)^3 \\ &+ \theta_0\eta[1 - \Gamma_0(e_1^E + e_2^E + e_3^E) + \eta/(2c_0)]. \end{aligned} \tag{4.37}$$

For the present loading mode and symmetry considerations, lateral elastic strains are equal, i.e.,

$$(F^E)_X^x = (F^E)_Y^y, \qquad e_1^E = e_2^E. \tag{4.38}$$

Three possibly nonzero stress components, two of which are equal, are obtained from (4.33) and (4.37):

$$\begin{aligned} P_1^1 = P_x^X = P_2^2 = P_y^Y &= (\mathsf{C}_{11} + \mathsf{C}_{12})e_1^E \\ &+ \mathsf{C}_{13}e_3^E + \frac{1}{2}B_0(2 - B_0')(\ln J^E)^2 - \theta_0\Gamma_0\eta, \\ P_3^3 = P_z^Z &= \frac{1}{1+\epsilon}\left[2\mathsf{C}_{13}e_1^E + \mathsf{C}_{33}e_3^E \right. \\ &\left. + \frac{1}{2}B_0(2 - B_0')(\ln J^E)^2 - \theta_0\Gamma_0\eta\right]. \end{aligned} \tag{4.39}$$

The conjugate thermodynamic force to $D = l\xi$ in (4.35) is then given by

$$\begin{aligned} Q = -\frac{1}{l}\left[2\frac{\Upsilon}{l}\xi + 2A\xi(1-\xi)(1-2\xi)\right. \\ \left. -2P_1^1(F^E)_X^x\frac{\partial(F^D)_X^X}{\partial\xi} - P_3^3(F^E)_Z^z\frac{\partial(F^D)_Z^Z}{\partial\xi}\right], \end{aligned} \tag{4.40}$$

where from (4.22),

$$\begin{aligned} \frac{\partial \boldsymbol{F}^D(\xi)}{\partial\xi} = \iota'(\xi)\left[\chi\mathbf{1} + \gamma_0\sum_{\alpha=1}^{6}\boldsymbol{s}^\alpha\otimes\boldsymbol{m}^\alpha\right. \\ + \frac{\gamma_0^2}{2}\left(\sum_{\alpha=1}^{6}\boldsymbol{s}^\alpha\otimes\boldsymbol{m}^\alpha\right)^2 \\ \left. + \frac{\gamma_0^3}{6}\left(\sum_{\alpha=1}^{6}\boldsymbol{s}^\alpha\otimes\boldsymbol{m}^\alpha\right)^3\right]. \end{aligned} \tag{4.41}$$

For shock loading in the Z direction, define the shock stress, positive in compression, as

$$P = -P_3^3 = -P_z^Z. \tag{4.42}$$

The treatment of surfaces of discontinuity of Sect. 3 applies here if direction X is replaced with direction Z. The thermodynamic driving force in (3.6) is, for uniaxial strain and a single scalar component of $\boldsymbol{D}$,

$$\zeta = \zeta_3 = T = 2\Upsilon\xi'. \tag{4.43}$$

For the present problem, the jump of scalar product $\boldsymbol{\zeta}\cdot\dot{\boldsymbol{D}}$ across the shock front becomes

$$[\![\boldsymbol{\zeta}\cdot\dot{\boldsymbol{D}}]\!] = 2\Upsilon l[\![\xi'\dot{\xi}]\!]. \tag{4.44}$$

Regions far ahead and far behind the shock front are assumed to be in equilibrium with respect to internal state. Across the front of presumed width l, the following diffuse interface approximations are imposed for the jump in order parameter gradient and its rate, whereby ξ increases from zero (i.e., its far upstream value $\xi^+ = 0$) to its downstream value ξ^- with decreasing material coordinate Z:

$$\begin{aligned} &\xi' \approx -\xi^-/l, \qquad \dot{\xi} \approx -\xi'\mathsf{D} \\ &\Rightarrow \quad 2\Upsilon l[\![\xi'\dot{\xi}]\!]/\mathsf{D} \approx -2(\Upsilon/l)(\xi^-)^2. \end{aligned} \tag{4.45}$$

Now let $\xi^- \to \xi$ in subsequent equations since ξ vanishes upstream. Analogs of Rankine-Hugoniot equations in (3.8) then become

$$\mathsf{v} = -\mathsf{D}\epsilon, \qquad P = \rho_0\mathsf{v}\mathsf{D}, \qquad U = \frac{1}{2}\rho_0\mathsf{v}^2 + 2\frac{\Upsilon}{l}\xi^2. \tag{4.46}$$

Downstream, the Ginzburg-Landau type equation (2.69) presumably holds with vanishing left side, i.e., $\dot{D} = l\dot{\xi} = 0$.

Forthcoming equations pertain to the downstream state. The shocked material in this state has nonzero

particle velocity v and density ρ, but it has null acceleration. Stress does not vary with time in regions far behind the shock so axial stress is of functional form $P = P(Z, D)$. The only significant equation in linear momentum balance (2.61) describes the direction of compressive loading: $a = z = 3$. Recalling that off-diagonal components of $\boldsymbol{P}$ vanish, momentum conservation in the downstream state requires $P^1_{1||1} = 0$. Substituting from (2.15) and (4.16), this results in the ordinary differential equation

$$\frac{\partial P(Z,D)}{\partial Z} + \frac{\partial P(Z,D)}{\partial D}\frac{\partial D}{\partial Z} + \frac{3B'(D)}{2B(D)}P\frac{\partial D}{\partial Z} = \frac{\mathrm{d}P}{\mathrm{d}Z} + P\frac{kD}{l}\frac{\mathrm{d}D}{\mathrm{d}Z} = 0. \tag{4.47}$$

The other two macroscopic linear momentum balance equations simply require that transverse stress components $P^X_x = P^Y_y$ are constant with respect to X and Y, respectively. These requirements are consistent with the assumed X and Y independence of solution fields for unaxial loading. The only pertinent equation in kinetic law (2.69) is, with $\dot{\xi} = 0$ for the downstream state,

$$\frac{\partial T(Z,D)}{\partial Z} + \left[\frac{\partial T(Z,D)}{\partial D} + \frac{3B'(D)}{2B(D)}T - P\frac{\partial^2\varphi(Z,D)}{\partial D^2}\right]\frac{\partial D}{\partial Z} - \frac{3B'(D)}{B(D)}U(Z,D) = Q(Z,D). \tag{4.48}$$

Kinetic coefficients L^{AB} are not needed. Substituting from (4.14) and (4.40), the two balance laws (4.47) and (4.48) become, for the equilibrium downstream shocked state,

$$\frac{\mathrm{d}P}{\mathrm{d}Z} = -kP\xi\frac{\mathrm{d}\xi}{\mathrm{d}Z}; \tag{4.49}$$

$$-P\frac{\partial^2\varphi}{\partial\xi^2}\xi' + 2\Upsilon l\xi'' - 2\frac{\Upsilon}{l}\xi - 2A\xi(1-\xi)(1-2\xi) = 2k\xi\left[U - \Upsilon l(\xi')^2\right] - 2P^1_1(F^E)^x_X\frac{\partial(F^D)^X_X}{\partial\xi} + P(F^E)^z_Z\frac{\partial(F^D)^Z_Z}{\partial\xi}. \tag{4.50}$$

Terms involving Weyl factor k result from dependence of the generalized pseudo-Finsler metric and corresponding Cartan's tensor coefficients on internal state. For Riemannian geometry, $k = 0$ and such terms vanish. Relations (4.49) and (4.50) are two coupled nonlinear differential equations wherein dependent field variables P^A_a, $(F^E)^a_\alpha$, $(F^D)^\alpha_A$, φ, ξ, and U all are ultimately functions of independent variable Z. However, the downstream state is assumed to be spatially homogeneous (in material coordinates) with regard to field variables, meaning that gradients with respect to Z vanish identically. Thus, differential equation (4.49) reduces to the trivial condition

$$P = -P^3_3 = \text{constant} \qquad \text{(downstream equilibrium)}, \tag{4.51}$$

with the value of this component and the equal and constant lateral stresses obeying constitutive equations in (4.39). Since a homogeneous order parameter field over the shocked portion of $\mathfrak{M}$ is in effect, $\xi' = 0$ and $\xi'' = 0$. Equation (4.50) then degenerates to the algebraic equation

$$-2\frac{\Upsilon}{l}\xi - 2A\xi(1-\xi)(1-2\xi) = 2k\xi U - 2P^1_1(F^E)^x_X\frac{\partial(F^D)^X_X}{\partial\xi} + P(F^E)^z_Z\frac{\partial(F^D)^Z_Z}{\partial\xi} \qquad \text{(downstream equilibrium)}. \tag{4.52}$$

If compressive deformation $\epsilon = F^3_3 - 1$ is prescribed as the condition denoting the intensity of the shock loading, equations (4.39), (4.46), and (4.52) can be solved simultaneously for the downstream state, where the form of internal energy in (2.65), (4.31), and (4.32) is also invoked. In other words, volume reduction is applied incrementally, and then the balance laws, jump conditions, and constitutive equations are solved simultaneously for the stresses, entropy, internal energy, and order parameter in the material behind the shock, as well as the particle velocity v and the shock speed D. Since $\iota'(0) = 0$ from (4.23), the entire right side of (4.52) vanishes when $\xi = 0$ according to (4.41). Because the left side also vanishes for $\xi = 0$, the nonlinear elastic solution (i.e., no inelastic deformation, no order parameter evolution) is clearly always a solution to (4.52). However, the nonlinear elastic solution is not necessarily the only solution, and it tends to be metastable, i.e., of higher total energy, than the alternative solution that exists above some nonzero strain and for which $\xi > 0$. For the present application to homogeneous downstream states, solutions are sought in practice by prescribing a value of $\xi = 1$ as an initial

guess at each applied strain increment and then decreasing ξ iteratively until the governing equations are satisfied simultaneously to within a tight tolerance. For more general applications requiring advanced numerical methods, it may be necessary to institute a perturbation in ξ somewhere in the domain as an initial condition to enable the inelastic solution, as has been invoked in phase field simulations of twinning (Clayton and Knap 2011a,b, 2013) that demonstrate a similar condition.

The terms proportional to the gradient of the order parameter, $\xi' = \mathrm{d}\xi/\mathrm{d}Z$, in (4.47) and (4.49) are ultimately a result of application of Rund's divergence theorem to (2.60) for pseudo-Finsler space, leading to contributions from the product of the trace of Cartan's tensor and the state variable gradient to the balance of linear momentum (Clayton 2017a). Physically, such terms can be interpreted as material or configurational forces induced by microstructure heterogeneity, since they have a similar, but not identical, effect on the linear momentum balance as those emerging from Eshelby-type forces (e.g., forces induced by local gradients in moduli) in elasticity theory (Marsden and Hughes 1994; Clayton 2011).

4.3 Material characteristics

Boron carbide (B_4C) is the particular material toward which the analysis of Sects. 4.1 and 4.2 is directed. In its ambient solid state, boron carbide is a low density crystalline ceramic of high hardness, high elastic stiffness, and low ductility. The usual crystal structure is rhombohedral. Material parameters used in the constitutive model, with supporting references, are listed in Table 1. If no reference or equation is listed for a particular value, the reference quoted above applies.

Most physical properties are self-explanatory, though those in the final six rows merit further discussion. The surface energy is that corresponding to fracture on $\{10\bar{1}1\}$ pyramidal planes of the single crystal as computed via first principles density functional theory (DFT) (Beaudet et al. 2015). The regularization length l and intrinsic surface energy are specified to have magnitudes corresponding to those for fracture since failure accompanies amorphization in experiments and since widths of amorphous zones observed experimentally are on the order of a nanometer (Yan et al. 2009; Grady 2011), of the same order as the fracture process zone length. The value of l in Table 1 is computed as the cohesive fracture process zone size over which the stress at a (mode II) crack tip degrades (Rice 1968; Clayton et al. 2012; Clayton 2017a):

$$l = 4\mu\Upsilon/[(1-\nu)\pi\sigma^2]. \tag{4.53}$$

Here, ν is Poisson's ratio and $\sigma \approx \frac{G_0}{2\pi}$ is the theoretical shear strength of the crystal (Clayton 2011). In the intended interpretation of the theory, as $\xi \to 1$ locally, the material progresses from glassy sheared state to a failed state at which inelastic deformation $\boldsymbol{F}^D$ saturates. Subsequently, the material is expected to undergo cavitation or some other means of fracture. Though not implemented in the present paper, a reduction in elastic coefficients would be needed to completely represent the fully failed state, as in phase field theories of fracture (Clayton and Knap 2014, 2015b). The surface energy Υ, which ultimately affects the regularization length l through (4.53), is assumed equal to the fracture energy, even though the material may be undergoing shear localization rather than (mode II) fracture for $\xi \in (0, 1)$. This assumption is made in part because the surface energy of the amorphous bands in the material is not well known. Thus, the same energy is employed to regularize a related mechanism (shear localization) as well as govern fracture itself when ξ reaches unity.

The Weyl transformation factor k is determined from the ratio of mass density of the crystalline phase to that of the glassy phase. This value is determined for the Finsler-geometric theory via consideration of (4.17) at $\xi = 1$. As in Clayton (2014a), invoked here is a 4% volume reduction (i.e., mass density increase) upon structure collapse commensurate with complete amorphization (Yan et al. 2009; Taylor 2015; An and Goddard 2015a), leading to $\exp(k/2) = 0.96 \Rightarrow k = 2\ln(0.96)$, consistent with (4.24). The barrier for phase transformation for a double well potential is $\frac{A}{16}$ at $\xi = 0.5$. This barrier is chosen as the difference between ground state energy of the most stable B_4C polytype and the energy of segregated elemental phases (boron and amorphous carbon) associated with structure collapse, 0.04 eV obtained from DFT (Fanchini et al. 2006). Finally, the inelastic shear strain γ_0 accommodated by amorphous slip bands at the onset of cavitation is obtained from results of atomic simulations, specifically molecular dynamics simulations with reactive force fields (RexFF) (An and Goddard 2015a). In these simulations, simple shearing at fixed volume on a pyrami-

Table 1 Physical properties of boron carbide

Property (Units)	Value	Description	References
C_{11} (GPa)	543	Second-order elastic constant	Clayton (2012a)
C_{12} (GPa)	131		
C_{13} (GPa)	64		
C_{14} (GPa)	−18		
C_{33} (GPa)	535		
C_{44} (GPa)	165		
B_0 (GPa)	237	Bulk modulus	
B_0'	4.7	Pressure derivative of bulk modulus	
G_0 (GPa)	236	Shear modulus	
c, a (nm)	1.21, 0.56	Lattice parameters	
ρ_0 (g/cm^3)	2.51	Mass density	
c_0 (MPa/K)	2.41	Specific heat	Clayton and Tonge (2015)
Γ_0	1.28	Grüneisen parameter	
θ_0 (K)	295	Ambient temperature	
Υ (J/m^2)	3.27	Surface energy	Beaudet et al. (2015)
l (nm)	0.97	Regularization length	(4.53)
$\exp(k/2)$	0.96	volume reduction (amorphization)	Yan et al. (2009), Clayton (2014a), An and Goddard (2015a)
A (GPa)	3.01	Transformation barrier	Fanchini et al. (2006)
γ_0	$\frac{1}{12}$	Inelastic shear accommodation	An and Goddard (2015a)

dal plane, specifically $[\bar{1}101](01\bar{1}\bar{1})$, resulted in a total difference in shear strain of $\approx \frac{1}{2}$ from the strain at emergence of amorphous bands on this plane at peak shear stress, followed by somewhat gradual softening behavior, and then finally failure by cavitation and shear fracture. Taking the emergence point in the Finsler continuum representation as that corresponding to initiation of nonzero ξ, and taking the failure point to correspond to $\xi \to 1$, slip accommodation for a single plane would thus be $\frac{1}{2}$ at saturation, i.e., at complete transformation just prior to rupture. In the present problem of compression along [0001], since six pyramidal planes support identical amorphous bands, it is assumed that degradation resulting from each plane is cumulative, leading to $\gamma_0 = \frac{1}{6} \cdot \frac{1}{2} = \frac{1}{12}$. The following caveat is noted, however. In atomic simulations reported in An and Goddard (2015a), steadily increasing shear stresses reaching local maxima in excess of 35–45 GPa, depending on possible volume relaxation, were observed, with substantial amorphization not taking place until shear strains in excess of 0.3 were applied. These magnitudes of shear stress and shear strain far exceed those predicted later in Sect. 4.4 for shock compression. However, boundary conditions differ substantially for the present work versus (An and Goddard 2015a), and the shear strengths reported in the latter are essentially upper bounds (i.e., theoretical maxima) since initial imperfections in the material are excluded by design. Acquisition of the present value of γ_0 motivated from An and Goddard (2015a) is perhaps inconsistent in light of the above discrepancies, but the present choice is deemed favorable to simply treating the constant as an adjustable parameter. Furthermore, the present choice is demonstrated later to enable accurate prediction of shock stress versus experimental data.

Importantly, in the present application of the Finsler theory to shock compression of boron carbide, parameter fitting by matching results of the model to experiments or third-party simulations is not necessary. All values shown in Table 1 are prescribed a priori and directly from experimental data or atomic calculations reported in the literature, though the aforementioned

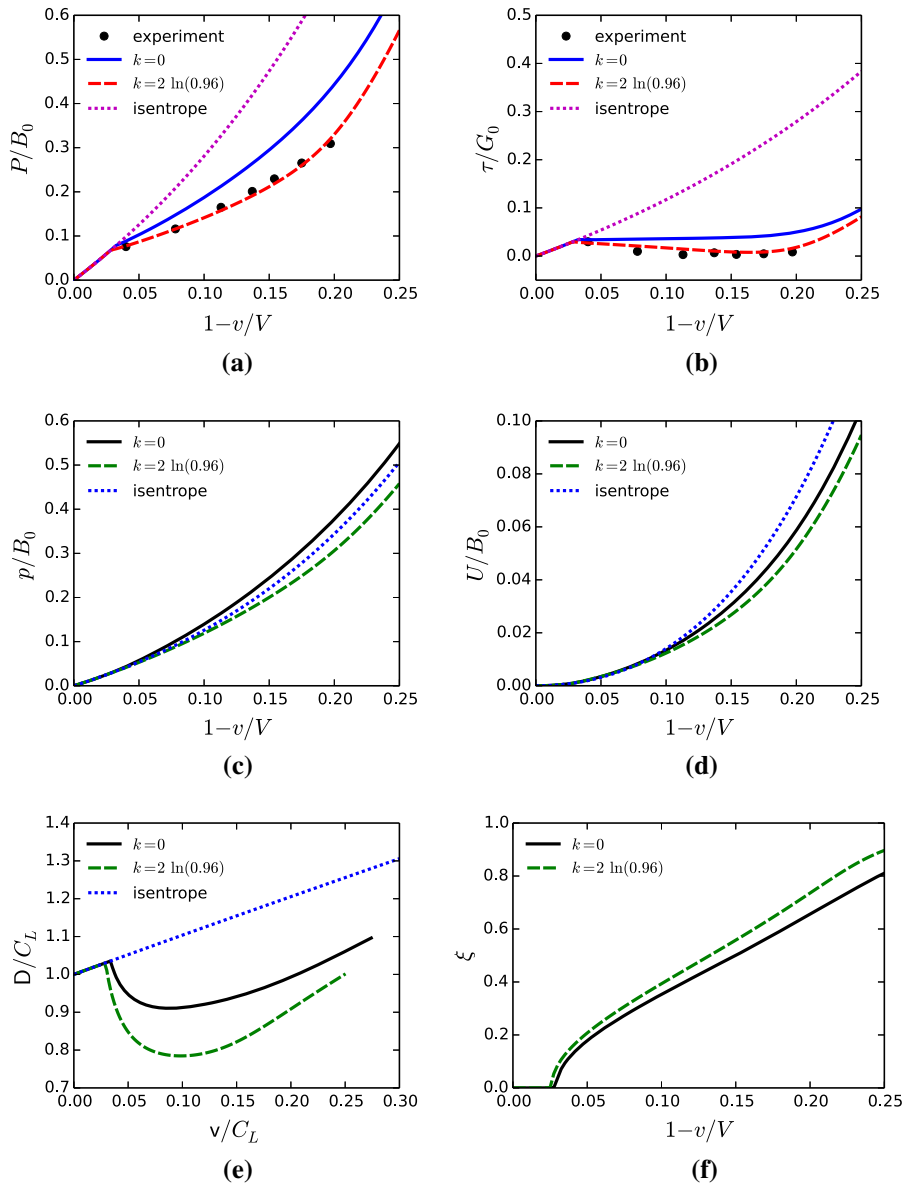

Fig. 1 Boron carbide, planar shock compression along c-axis **a** axial (shock) stress and experimental data Vogler et al. (2004) **b** shear stress and experimental data Vogler et al. (2004) **c** Cauchy pressure **d** internal energy **e** shock velocity versus particle velocity **f** order parameter $\xi = D/l$

caveat regarding γ_0 is recalled. Thus, model outcomes reported later in Sect. 4.4 are considered fully predictive.

4.4 Solutions and interpretations

Solutions to the planar shock problem for boron carbide are illustrated in Fig. 1 which is analyzed in detail in the following discussion. Axial shock stress P normalized by the bulk modulus B_0 is shown versus compression in Fig. 1a, where $J = v/V = F_3^3 = 1 + \epsilon$ is the ratio of volume after compression to the initial volume. Results for the physically realistic case invoking inelastic volume reduction in conjunction with amorphization, i.e., densification, correspond to the Weyl scaling parameter $k = 2\ln(0.96)$ as listed in Table 1. Results for $k = 0$ omit the density difference between crystal and glass phases. Experimental data correspond to planar impact tests on the polycrystalline ceramic (Vogler et al. 2004); experimental shock data for single crystals is absent in the literature. The isentrope corresponding to purely elastic uniaxial strain of the single crystal is obtained by setting $\xi = 0$ throughout a correspond-

ing static compression process. Excellent agreement between predictions of the present model with $k < 0$ and experimental data is obvious, thereby lending confidence to the current theory and solution, at least for this particular application. The Finsler solutions and experiment all suggest a Hugoniot Elastic Limit (HEL, i.e., stress P at the initial yield point) of $P \approx 18$ GPa at $v/V \approx 0.96$. Post-yielding, shock stress is higher for the case when inelastic density changes are omitted ($k = 0$) than when they are included ($k < 0$). Stress P is largest for the isentrope, as expected, since inelastic deformation by shear localization and volume collapse that would otherwise relieve elastic strain is excluded.

Dynamic shear strength τ normalized by the shear modulus $G_0 = \frac{1}{2}(\mathsf{C}_{33} - \mathsf{C}_{13})$ is shown versus compression in Fig. 1b, where specifically

$$\tau = \frac{1}{2}|\sigma_3^3 - \sigma_1^1| = \frac{1}{2}|\sigma_3^3 - \sigma_2^2| \tag{4.54}$$

is half the difference between longitudinal and transverse components of Cauchy stress $\boldsymbol{\sigma}$. Close agreement between the present solution with $k < 0$ and experiment (Vogler et al. 2004) is evident. Shear stress at the HEL is $\tau \approx 7$ GPa (Vogler et al. 2004); strength degrades then increases slightly with increasing compression beyond this point for the present model with $k < 0$ as well as experiment. As is the case for axial stress, shear stress is highest at larger compression for the isentropic solution (no shear accommodation by slip/inelasticity), with τ for the Finsler model with $k = 0$ falling in between the other two cases at compressive strains exceeding that at the HEL. As evidenced by the drop in shear strength upon attainment of the HEL, both the experimental data and the Finsler solutions demonstrate how boron carbide softens and fails in shear under compressive loading. In the real material, at large compressive deformations, friction at internal surfaces may contribute to shear strength; this effect is omitted in the present application of the theory.

A limitation of the present shock solutions is the predicted deviation from realistic behavior at volumetric compressions exceeding 20%, for which an upturn in shear stress is evident in Fig. 1b. This upturn is a result of the contribution from internal state ξ to (4.22) approaching saturation, such that inelastic shear deformation is no longer able to sufficiently offset total deviatoric deformation, leading to an increase in elastic strain and shear stress. The curvature of the curve of total axial stress P in Fig. 1a likewise becomes too great at large compression. The problem could be remedied by permitting elastic stiffness coefficients (e.g., shear moduli but not compressive bulk modulus) to degrade with increasing ξ, as in phase field fracture models (Clayton and Knap 2014, 2015a), above some threshold. Such model additions should be enabled in future work for more general materials failure problems.

Figure 1c reports the Cauchy pressure p normalized by the ambient bulk modulus, computed via

$$p = -\frac{1}{3}(\sigma_1^1 + \sigma_2^2 + \sigma_3^3) = -\frac{1}{3}(2\sigma_1^1 + \sigma_3^3) = P - 2\tau, \tag{4.55}$$

recalling that $P = -\sigma_3^3$. The same three cases are addressed: the Finsler model with no phase densification ($k = 0$), the Finsler model with realistic inelastic densification [$k = 2\ln(0.96)$], and isentropic compression ($\xi = 0$). Complementary predictions for the internal energy per unit reference volume U are shown in Fig. 1d. Results of the three cases coincide for compressive loading below the HEL, i.e., for $v/V \gtrsim 0.96$. For larger compression, pressure is largest for the Finsler result with $k = 0$, followed by the isentrope, and then smallest for the Finser result with $k < 0$. Comparing Fig. 1a with c, the shock stress P only slightly exceeds the Cauchy pressure p for compressive volume reductions in the range $0.95 \geq v/V \geq 0.80$ where shear stress is relatively small (Fig. 1b). Ordering of internal energy is interchanged between the cases of isentrope and Finsler result with $k = 0$. In particular, results for internal energy demonstrate that the Finsler solutions are stable, i.e., of lower total internal energy, relative to the isentropic elastic solution that has the largest energy. This is an important finding since the isentropic solution is always a (possibly non-unique) solution to the static governing equations in the present constitutive model. Pressure is larger in the Finsler result for $k = 0$ than that of the isentropic solution because of thermoelastic coupling and substantial entropy production. The increase in pressure from entropy production is more than offset by a decrease in pressure with densification for the Finsler result with $k = 2\ln(0.96)$. Normalized temperatures θ/θ_0 at 20% compression for the shock solutions are 4.0 and 4.1 for $k = 0$ and $k = 2\ln(0.96)$, compared to 1.3 for the isentropic solution. The temperature rise and pressure for the shocked material in the absence of inelasticity (i.e., for a nonlinear elastic shock, physically valid only for shock

stresses up to the HEL) only slightly exceed those of the isentrope; this has been demonstrated elsewhere in calculations for a number of brittle ceramics and minerals invoking nonlinear logarithmic thermoelasticity (Clayton 2014c, b; Clayton and Tonge 2015). A contribution to tensile pressure in amorphous bands leading to cavitation has been noted in prior atomic (An and Goddard 2015a) and continuum (Clayton 2016b) model results for shear loading.

Shock velocity D is shown versus particle velocity v in the compressed state in Fig. 1e, with both velocities normalized by the longitudinal elastic wave speed $C_L = \sqrt{\mathsf{C}_{33}/\rho_0}$. The same three cases are considered, with the isentropic solution giving a steadily increasing shock speed with increasing particle velocity corresponding to increasing shock stress or decreasing volume. This increasing isentropic shock speed is a result of elastic nonlinearity, specifically the increasing tangent longitudinal modulus with increasing elastic compression. When the shock stress exceeds the HEL for the other two cases, a drop in shock velocity occurs commensurate with a loss of tangent stiffness and shear strength (Fig. 1b). The largest drop in shock velocity occurs for the realistic model with $k < 0$. Shock velocity reaches a local minimum then increases with increasing compressive strain or particle velocity. The same trends in shock velocity versus particle velocity are evident in experimental data of Vogler et al. (2004) and in many, but not all, experimental and quantum molecular results reported in Taylor (2015).

Finally, the order parameter physically connected to shear accommodation by amorphous bands is shown versus compressive strain in Fig. 1f for the Finsler model with $k = 0$ and $k = 2\ln(0.96)$. At small compressive strains $v/V \gtrsim 0.97$, the order parameter $\xi = 0$ and the response is isentropic and elastic. A rapid increase occurs for each case around the HEL, followed by a more gradual increase at larger compressive strains or higher shock stresses. The magnitude of ξ for the case with densification upon phase transformation slightly exceeds that for the case with $k = 0$ since the magnitude of the elastic driving force $\partial W/\partial\xi$ promoting evolution of ξ is greater under compressive loading when volume reduction due to amorphization is included in the constitutive model. In other words, volume reduction due to phase transformation accommodates strain that otherwise would be accommodated elastically leading to an increase in pressure and volumetric strain energy density. Notice that in each case, the order parameter increases towards, but never attains, a value of unity with increasing applied strain. The reason for this arises from a nonzero thermodynamic force (Q) contribution from the quadratic term in ξ entering the energy functional, leading to the first term on the left side of (4.52) that does not vanish at $\xi = 1$. Such an effect is also present in phase field models of fracture that employ the standard quadratic contribution from an order parameter to the energy density (Clayton and Knap 2015a; Borden et al. 2012). Homogeneous solutions for quasi-static fracture problems demonstrate order parameter values that asymptotically approach unity with increasing strain, with the rate of approach dependent upon normalized regularization length (Clayton and Knap 2015a).

Recent work involving either quantum mechanics (DFT) or molecular dynamics simulations (ReaxFF) (An and Goddard 2015a, b; Tang et al. 2015) has provided insight into effects of composition and loading direction (with respect to the crystal structure) on resistance to shear localization, subsequent cavitation, and failure of boron-based ceramic crystals under (simple) shear loading with periodic boundary conditions. In particular, computationally designed atomic structures featuring layers of B_4C and boron suboxide (B_6O) have demonstrated increased overall ductility relative to more brittle pure boron carbide crystals (Tang et al. 2015). It is suggested here that improvements in fundamental physical properties such as surface energy Υ, glassy phase characteristics (e.g., mass density change quantified by k and energy change quantified by A), and shear slip accommodation by amorphous banding quantified by γ_0 may be possible via tailoring of boron-based ceramic compositions and structures. Conversely, as indicated by quantum mechanical results (Taylor 2015), physical properties such as resistance to structure collapse may be deleteriously affected via changes in atomic structure, for example lattice site vacancies.

Predictions of the present continuum model of shock compression demonstrating effects of variations of the aforementioned fundamental properties Υ, A, and γ_0 are shown in Fig. 2. Specifically, Fig. 2a shows shock stress P, the fundamental mechanical force resisting uniaxial shock compression, while Fig. 2b shows shear stress (i.e., strength) τ, which is thought to be a primary indicator of resistance of a ceramic material to ballistic penetration, i.e., penetration by an impacting projectile (Bourne 2008; Clayton 2015b). Results labeled

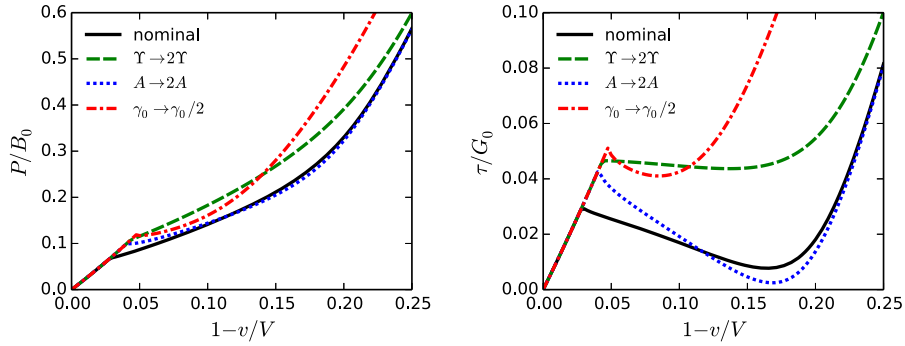

Fig. 2 Effects of surface energy Υ, transformation barrier A, and shear band strain γ_0 on **a** axial (shock) stress **b** shear stress

as "nominal" correspond to the most physically realistic model considered here with $k = 2\ln(0.96)$, as discussed already in the context of Fig. 1. Recall that effects of k have already been reported in Fig. 1, demonstrating for $k = 0$ an increase in shock stress and shear strength relative to the nominal case. General increases in shock stress and, more evidently, shear strength are apparent with increases in fracture energy and transformation energy, and with decreases in γ_0. The total driving force for transformation decreases commensurately with such property variations, thereby inhibiting the trajectory of the shocked substance towards a fully amorphous and subsequently ruptured state. Noteworthy is the dramatic increase in strength with decreasing γ_0, clarifying remarks from Sect. 4.3 that this parameter is not a measure of ductility of the crystal, but rather is better labeled as a measure of the shear damage associated with amorphous band formation and multiplication, somewhat analogous to the overall inelastic shear strain accommodated by crack opening displacement for mode II fracture. The greatest potential increases to strength correspond to halving of this parameter and doubling of surface energy Υ. Less improvement results from doubling of transformation (double well potential) barrier A, which affords almost no strength increase at very large compressions relative to the nominal case.

The example considered herein has imposed homogeneous deformation and internal state behind the shock front, with total deformation one-dimensional. This example is deemed a requisite early step towards understanding and eventually validating a novel and mathematically sophisticated theory. Future work will consider multi-dimensional problems involving heterogeneous deformation and spatial gradients of state variables, including explicit localization phenomena. More advanced numerical methods will be needed to solve such problems whose solutions should provide additional insight into material performance, i.e., resistance to failure.

5 Conclusions

A theory of Finsler-geometric continuum mechanics developed recently by the author using variational principles has been extended to address dynamics—material inertia, order parameter evolution, internal energy conservation—as well as temperature change and entropy production for the adiabatic case. Jump conditions pertinent to exchange of mass, linear momentum, and energy across a shock front moving at steady speed have been derived. The theory has been invoked to describe stress-induced phase transitions and shear inelasticity in boron carbide subjected to planar impact-type loading. All parameters in the model are obtained from fundamental experiments or results of atomic simulations from the literature, without further calibration. Predictions of the model for shock stress, shear strength, and shock characteristics agree closely with experimental data when the conformal transformation accounting for densification upon phase change is included. In order to guide efforts towards design of new compositions of boron-based ceramics, parameter studies predicting effects of variations in surface energy, transformation energy, and shear accommodation have been reported. Results suggest that, in increasing order of improved dynamic shear strength, the following structural property changes should be sought: increases in the energy barrier for amorphization, decreases in the density of the glassy phase,

increases in the surface energy, and decreases in the post-peak shear localization strain.

Acknowledgements This paper was initiated while the author served as a visiting research fellow at Columbia University, specifically in the Department of Civil Engineering and Engineering Mechanics of the Fu Foundation School of Engineering and Applied Science in New York, NY, USA. The author acknowledges the courtesy of Dr. WaiChing (Steve) Sun for hosting his sabbatical visit at Columbia University in 2016.

References

Allen SM, Cahn JW (1979) A microscopic theory for antiphase boundary motion and its application to antiphase domain coarsening. Acta Metall 27:1085–1095

Amari S (1962) A theory of deformations and stresses of ferromagnetic substances by Finsler geometry. In: Kondo K (ed.) RAAG Memoirs, vol. 3, Tokyo, pp 257–278

An Q, Goddard WA (2015a) Atomistic origin of brittle failure of boron carbide from large-scale reactive dynamics simulations: suggestions toward improved ductility. Phys Rev Lett 115:105051

An Q, Goddard WA (2015b) Boron suboxide and boron subphosphide crystals: hard ceramics that shear without brittle failure. Chem Mater 27:2855–2860

Aslan O, Cordero NM, Gaubert A, Forest S (2011) Micromorphic approach to single crystal plasticity and damage. Int J Eng Sci 49:1311–1325

Bammann DJ, Solanki KN (2010) On kinematic, thermodynamic, and kinetic coupling of a damage theory for polycrystalline material. Int J Plast 26:775–793

Barton NR, Winter NW, Reaugh JE (2009) Defect evolution and pore collapse in crystalline energetic materials. Model Simul Mat Sci Eng 17:035003

Beaudet TD, Smith JR, Adams JW (2015) Surface energy and relaxation in boron carbide ($10\bar{1}1$) from first principles. Solid State Commun 219:43–47

Bejancu A (1990) Finsler Geom Appl. Ellis Horwood, New York

Borden MJ, Verhoosel CV, Scott MA, Hughes TJR, Landis CM (2012) A phase-field description of dynamic brittle fracture. Comput Methods Appl Mech Eng 217:77–95

Bourne NK (2008) The relation of failure under 1D shock to the ballistic performance of brittle materials. Int J Impact Eng 35:674–683

Bronkhorst CA, Cerreta EK, Xue Q, Maudlin PJ, Mason TA, Gray GT (2006) An experimental and numerical study of the localization behavior of tantalum and stainless steel. Int J Plast 22:1304–1335

Bronkhorst CA, Gray GT, Addessio FL, Livescu V, Bourne NK, MacDonald SA, Withers PJ (2016) Response and representation of ductile damage under varying shock loading conditions in tantalum. J Appl Phys 119:085103

Capriz G (1989) Continua with microstructure. Springer, New York

Casey J (2011) On the derivation of jump conditions in continuum mechanics. Int J Struct Changes Sol 3:61–84

Chen M, McCauley JW, Hemker KJ (2003) Shock-induced localized amorphization in boron carbide. Science 299:1563–1566

Cheng J, Ghosh S (2013) Computational modeling of plastic deformation and shear banding in bulk metallic glasses. Comput Mater Sci 69:494–504

Clayton JD, McDowell DL, Bammann DJ (2004a) A multiscale gradient theory for elastoviscoplasticity of single crystals. Int J Eng Sci 42:427–457

Clayton JD, Bammann DJ, McDowell DL (2004b) Anholonomic configuration spaces and metric tensors in finite strain elastoplasticity. Int J Non Linear Mech 39:1039–1049

Clayton JD (2005a) Dynamic plasticity and fracture in high density polycrystals: constitutive modeling and numerical simulation. J Mech Phys Solids 53:261–301

Clayton JD (2005b) Modeling dynamic plasticity and spall fracture in high density polycrystalline alloys. Int J Solids Struct 42:4613–4640

Clayton JD, McDowell DL, Bammann DJ (2006) Modeling dislocations and disclinations with finite micropolar elastoplasticity. Int J Plast 22:210–256

Clayton JD (2009) A continuum description of nonlinear elasticity, slip and twinning, with application to sapphire. Proc R Soc Lond A 465:307–334

Clayton JD (2010) Deformation, fracture, and fragmentation in brittle geologic solids. Int J Fract 163:151–172

Clayton JD (2011) Nonlinear mechanics of crystals. Springer, Dordrecht

Clayton JD (2012a) Towards a nonlinear elastic representation of finite compression and instability of boron carbide ceramic. Philos Mag 92:2860–2893

Clayton JD (2012b) On anholonomic deformation, geometry, and differentiation. Math Mech Solids 17:702–735

Clayton JD, Kraft RH, Leavy RB (2012) Mesoscale modeling of nonlinear elasticity and fracture in ceramic polycrystals under dynamic shear and compression. Int J Solids Struct 49:2686–2702

Clayton JD (2013a) Mesoscale modeling of dynamic compression of boron carbide polycrystals. Mech Res Commun 49:57–64

Clayton JD (2013b) Nonlinear Eulerian thermoelasticity for anisotropic crystals. J Mech Phys Solids 61:1983–2014

Clayton JD (2014a) Phase field theory and analysis of pressure-shear induced amorphization and failure in boron carbide ceramic. AIMS Mater Sci 1:143–158

Clayton JD (2014b) Analysis of shock compression of strong single crystals with logarithmic thermoelastic-plastic theory. Int J Eng Sci 79:1–20

Clayton JD (2014c) Finite strain analysis of shock compression of brittle solids applied to titanium diboride. Int J Impact Eng 73:56–65

Clayton JD (2014d) Differential geometry and kinematics of continua. World Scientific, Singapore

Clayton JD (2014e) Shock compression of metal crystals: a comparison of Eulerian and Lagrangian elastic-plastic theories. Int J Appl Mech 6:1450048

Clayton JD (2015a) On Finsler geometry and applications in mechanics: review and new perspectives. Adv Math Phys 2015:828475

Clayton JD (2015b) Penetration resistance of armor ceramics: dimensional analysis and property correlations. Int J Impact Eng 85:124–131

Clayton JD (2015c) Crystal thermoelasticity at extreme loading rates and pressures: analysis of higher-order energy potentials. Extreme Mech Lett 3:113–122
Clayton JD (2016a) Finsler-geometric continuum mechanics. Technical Report ARL-TR-7694, US Army Research Laboratory, Aberdeen Proving Ground MD
Clayton JD (2016b) Finsler-geometric continuum mechanics and the micromechanics of fracture in crystals. J Micromech Mol Phys 1:164003
Clayton JD (2016c) Dimensional analysis and extended hydrodynamic theory applied to long-rod penetration of ceramics. Def Technol 12:334–342
Clayton JD (2017a) Finsler geometry of nonlinear elastic solids with internal structure. J Geom Phys 112:118–146
Clayton JD (2017b) Generalized finsler geometric continuum physics with applications in fracture and phase transformations. Zeitschrift fur Angewandte Mathematik und Physik (ZAMP) 68:9
Clayton JD, Knap J (2011a) A phase field model of deformation twinning: nonlinear theory and numerical simulations. Phys D 240:841–858
Clayton JD, Knap J (2011b) Phase field modeling of twinning in indentation of transparent single crystals. Model Simul Mat Sci Eng 19:085005
Clayton JD, Knap J (2013) Phase field analysis of fracture induced twinning in single crystals. Acta Mater 61:5341–5353
Clayton JD, Knap J (2014) A geometrically nonlinear phase field theory of brittle fracture. Int J Fract 189:139–148
Clayton JD, Knap J (2015a) Nonlinear phase field theory for fracture and twinning with analysis of simple shear. Philos Mag 95:2661–2696
Clayton JD, Knap J (2015b) Phase field modeling of directional fracture in anisotropic polycrystals. Comput Mater Sci 98:158–169
Clayton JD, McDowell DL (2003) A multiscale multiplicative decomposition for elastoplasticity of polycrystals. Int J Plast 19:1401–1444
Clayton JD, Tonge A (2015) A nonlinear anisotropic elastic-inelastic constitutive model for polycrystalline ceramics and minerals with application to boron carbide. Int J Solids Struct 64–65:191–207
Curran DR, Seaman L, Cooper T, Shockey DA (1993) Micromechanical model for comminution and granular flow of brittle material under high strain rate application to penetration of ceramic targets. Int J Impact Eng 13:53–83
Fanchini G, McCauley JW, Chhowalla M (2006) Behavior of disordered boron carbide under stress. Phys Rev Lett 97:035502
Foulk JW, Vogler TJ (2010) A grain-scale study of spall in brittle materials. Int J Fract 163:225–242
Grady DE (2011) Adiabatic shear failure in brittle solids. Int J Impact Eng 38:661–667
Hildebrand FE, Miehe C (2012) A phase field model for the formation and evolution of martensitic laminate microstructure at finite strains. Philos Mag 92:4250–4290
Levitas VA, Levin VA, Zingerman KM, Freiman EI (2009) Displacive phase transitions at large strains: phase-field theory and simulations. Phys Rev Lett 103:025702
Levitas VI (2014) Phase field approach to martensitic phase transformations with large strains and interface stresses. J Mech Phys Solids 70:154–189
Li S, Liu W-K, Qian D, Guduru PR, Rosakis AJ (2001) Dynamic shear band propagation and micro-structure of adiabatic shear band. Comput Methods Appl Mech Eng 191:73–92
Li S, Wang G (2004) On damage theory of a cohesive medium. Int J Eng Sci 42:861–885
Lloyd JT, Clayton JD, Austin RA, McDowell DL (2014a) Plane wave simulation of elastic-viscoplastic single crystals. J Mech Phys Solids 69:14–32
Lloyd JT, Clayton JD, Becker R, McDowell DL (2014b) Simulation of shock wave propagation in single crystal and polycrystalline aluminum. Int J Plast 60:118–144
Luscher DJ, Bronkhorst CA, Alleman CN, Addessio FL (2013) A model for finite-deformation nonlinear thermomechanical response of single crystal copper under shock conditions. J Mech Phys Solids 61:1877–1894
Marsden JE, Hughes TJR (1994) Mathematical foundations of elasticity. Dover, New York
Minguzzi E (2014) The connections of pseudo-Finsler spaces. Int J Geom Methods Mod Phys 11:1460025
Rice JR (1968) Mathematical analysis in the mechanics of fracture. In: Liebowitz H (ed) Fracture: an advanced treatise. Academic Press, New York, pp 191–311
Rund H (1975) A divergence theorem for Finsler metrics. Monatshefte fur Mathematik 79:233–252
Saczuk J (1996) Finslerian foundations of solid mechanics. Polskiej Akademii Nauk, Gdansk
Shahba A, Ghosh S (2016) Crystal plasticity FE modeling of Ti alloys for a range of strain-rates. Part I: a unified constitutive model and flow rule. Int J Plast 87:48–68
Stumpf H, Saczuk J (2000) A generalized model of oriented continuum with defects. Zeitschrift für Angewandte Mathematik und Mechanik (ZAMM) 80:147–169
Sun W, Mota A (2014) A multiscale overlapped coupling formulation for large-deformation strain localization. Comput Mech 54:803–820
Tang B, An Q, Goddard WA (2015) Improved ductility of boron carbide by microalloying with boron suboxide. J Phys Chem C 119:24649–24656
Taylor DE, McCauley JW, Wright TW (2012) The effects of stoichiometry on the mechanical properties of icosahedral boron carbide under loading. J Phys Condens Matter 24:505402
Taylor DE (2015) Shock compression of boron carbide: a quantum mechanical analysis. J Am Ceram Soc 98:3308–3318
Vogler TJ, Reinhart WD, Chhabildas LC (2004) Dynamic behavior of boron carbide. J Appl Phys 95:4173–4183
Vogler TJ, Clayton JD (2008) Heterogeneous deformation and spall of an extruded tungsten alloy: plate impact experiments and crystal plasticity modeling. J Mech Phys Solids 56:297–335
Weyl H (1952) Space-time-matter, 4th edn. Dover, New York
Xu X-P, Needleman A (1994) Numerical simulations of fast crack growth in brittle solids. J Mech Phys Solids 42:1397–1434
Yan XQ, Tang Z, Zhang L, Guo JJ, Jin CQ, Zhang Y, Goto T, McCauley JW, Chen MW (2009) Depressurization amorphization of single-crystal boron carbide. Phys Rev Lett 102:075505